# ATP10A promotes endothelial cell insulin sensitivity and protects against diet-induced dyslipidemia in female mice

**Adriana C. Norris[1], Eugenia M. Yazlovitskaya[1], Lin Zhu[2], Bailey S. Rose[3,4,5,6,7], Alex Mansueto[1], Katherine N. Gibson-Corley[8], Jody C. May[3,4,5,6,7], John A. McLean[3,4,5,6,7], John M. Stafford [2,9,10], Todd R. Graham[1]**

[1]Department of Biological Sciences, Vanderbilt University, Nashville, Tennessee, USA.[2]Division of Endocrinology, Diabetes and Metabolism, Vanderbilt University Medical Center, USA. [3]Department of Chemistry, [4]Center for Innovative Technology, [5]Vanderbilt-Ingram Cancer Center, [6]Vanderbilt Institute of Chemical Biology, [7]Vanderbilt Institute for Integrative Biosystems Research and Education, Vanderbilt University, Nashville, Tennessee, USA. [8]Division of Comparative Medicine, Department of Pathology, Microbiology and Immunology, Vanderbilt University Medical Center, Nashville, Tennessee, USA.[9]Tennessee Valley Healthcare System, Veterans Affairs, Nashville, Tennessee, USA. [10]Department of Molecular Physiology and Biophysics, Vanderbilt University, Tennessee, USA.

**Abstract**

Endothelial dysfunction is strongly associated with metabolic and cardiovascular disease but how genetic and environmental factors intersect to promote disease progression remains elusive. Genetic association studies have linked ATP10A and closely related type IV P-type ATPases (P4-ATPases) to insulin resistance and vascular complications, such as atherosclerosis. Here, we generated *Atp10A* knockout mice and show that *Atp10A* deficiency results in female-specific dyslipidemia, independent of diet-induced obesity, characterized by elevated plasma triglycerides, free fatty acids and cholesterol, as well as altered VLDL and HDL properties. We also observed increased circulating levels of several sphingolipid species and reduced eicosanoids and bile acids levels. Additionally, the *Atp10A*$^{-/-}$ mice display hepatic insulin resistance without perturbations to whole-body glucose homeostasis. ATP10A is expressed in vascular and lymphatic endothelial cells, where reduced expression causes hyperactive insulin signaling at basal insulin levels and an inability to properly respond to added insulin. This unique form of insulin resistance suggests that ATP10A promotes insulin receptor desensitization to maintain endothelial cell insulin sensitivity. These findings may lead to therapeutic approaches to enhance ATP10A expression and improve vascular health and lipid metabolic profiles.

**Introduction**

The metabolic syndrome is a complex condition that affects 33% of Americans (1) and on a global scale, over 1 billion people (2). This syndrome is characterized by abdominal obesity, insulin resistance, hypertension, and dyslipidemia, and an increased risk of developing type 2 diabetes mellitus and atherosclerotic cardiovascular disease (ASCVD) (3). By promoting oxidative stress and inflammation, these conditions can cause damage to the vascular endothelium (4,5). A damaged vascular endothelium is more susceptible to atherosclerosis,

aneurysms, and arteriosclerosis, which increases risks of developing chronic diseases. It is well established that vasculature damage can be a consequence of these disorders, interestingly, there is also evidence for vasculature dysfunction playing a causal role in promoting these disorders (6). Therefore, there is a need to develop a comprehensive understanding of the 'crosstalk' that occurs between the endothelium and resident tissues in the context of the metabolic syndrome. This will provide insight into how to maintain a healthy vasculature as well as inform the development of therapeutics that can help heal a damaged vasculature.

ATP10A is a potential effector of endothelial cell (EC) and tissue crosstalk. ATP10A shows the highest expression in human arterial tissue (GTEx, a public resource with human expression data) and murine brain ECs (Tabula Muris, a single cell transcriptome database from *Mus musculus* (7)). Commonly found variants in *ATP10A* have been linked to increased risk of insulin resistance (8) and variants within a related gene, *ATP10D*, have been linked to increased atherosclerosis risk (9). ATP10A and ATP10D are P4-ATPases, also known as lipid flippases, that translocate lipids from the exoplasmic or luminal leaflets to cytosolic leaflets of cell membranes. This creates an asymmetric distribution of lipids within membranes that has several implications for the cell (10), including in apoptosis (11), vesicular trafficking (12), and signal transduction (13).

Interestingly, most of the 14 human P4-ATPases have established roles in disease, such as in severe neurological disorders and intrahepatic cholestasis (14). These enzymes transport specific lipid substrates, which are closely related to their cellular and physiological functions. ATP10A flips phosphatidylcholine (PC) (15) and glucosylceramide (GlcCer) (16). PC has structural roles in membranes (17) and is involved in protein trafficking (18). Its metabolites, such as lysophosphatidylcholine (LysoPC), arachidonic acid (AA), and eicosanoids produced from AA, have roles in modulating inflammation and various disease states (19-23). GlcCer is a bioactive lipid that can also affect insulin signaling and energy homeostasis (24), as well as inflammation (25). Inhibiting GlcCer synthase enhances insulin sensitivity (26) and protects

against cardiac hypertrophy (27). GlcCer can be broken down into ceramide or built up into gangliosides, which also have established roles in metabolism (28-30).

Previous reports suggested a role for murine ATP10A in diet-induced obesity and insulin resistance, however, the mouse model used in these studies contained a large, irradiation-induced chromosomal deletion that included *Atp10A* (previously named *Atp10C)* and several other genes (31,32). End-point mapping of a nested deletion series implicated *Atp10A* in the metabolic defects but whether an *Atp10A*-specific knockout is sufficient to cause insulin resistance has not been determined. Homozygosity of the irradiation-induced deletion resulted in embryonic lethality, but heterozygous mice that inherited the chromosomal deletion maternally displayed more severe metabolic phenotypes compared to those who inherited the deletion paternally. This observation suggested that the *Atp10A* locus was imprinted to suppress expression of the paternal allele, however several studies failed to detect imprinted expression of the *ATP10A* gene (33-35). It appears that *ATP10A* expression pattern is complex and dependent on multiple factors including gender, genetic background, and tissue type.

Although correlations between *ATP10A* deficiency and insulin resistance, diet-induced obesity, and glucose uptake (36) have been reported, it is unclear whether this flippase plays a causative role in these processes or has any function in ECs, where its expression has been detected. Here, we generated a gene-specific deletion and tested the impact of *Atp10A* deficiency in mice during high fat diet (HFD) feeding. *Atp10A* deficient mice display female-specific diet-induced dyslipidemia, disruptions in liver insulin signaling, and broad changes to lipid metabolism. Additionally, we found that ATP10A is expressed in ECs in liver and visceral fat and that ATP10A knockdown in cultured ECs results in perturbations to insulin-dependent signaling as well as alterations to the regulation of an important vasodilator, endothelial nitric oxide synthase (eNOS), suggesting a potential role for ATP10A in endothelial and resident tissue ‘crosstalk’ as well as in vascular maintenance and health.

## Results

*Atp10A deficiency in mice does not affect body composition after high fat feeding.* To develop the *Atp10A*$^{-/-}$ mice, we created a gene-specific knockout allele of *Atp10A* in the C57BL/6J background using CRISPR/Cas9 guide RNA sequences targeted to regions flanking exon 2 (Figure 1A). To test the potential impact of *Atp10A* on weight gain, we placed male and female WT (*Atp10A*$^{+/+}$) and KO (*Atp10A*$^{-/-}$) mice on a HFD for 12 weeks. We found that there was no significant difference in weight gain in males or females based on genotype (Figure 1B). We next examined body composition and size and found that male and female mice did not display a difference in % lean mass (Figure 1C) or % fat mass (Figure 1D) based on genotype. Additionally, male mice did not exhibit changes in body length based on genotype, however, female *Atp10A*$^{-/-}$ mice had smaller bodies compared to WT mice (Supplemental Figure 1A). We did not observe any changes in tissue mass (Supplemental Figure 1B) or food intake and energy expenditure (Supplemental Figure 2) in female mice based on genotype. To distinguish between the metabolic effects of *Atp10A* deficiency versus HFD feeding, we measured weight gain, body composition, and body length in female mice on normal chow; and found no significant differences based on genotype (Supplemental Figure 3A-D). Altogether, these results indicate that *Atp10A* deficiency does not cause diet-induced obesity under the conditions tested.

*Atp10A deficiency does not affect whole-body glucose homeostasis in female mice.* To assess the influence of *Atp10A* on glucose homeostasis, we fasted mice for 5 hours and measured their fasting blood glucose, insulin levels, and performed an oral glucose tolerance test (OGTT). We found no significant difference in fasting blood glucose (Figure 1E), fasting insulin levels (Figure 1F), or in the kinetics of glucose clearance following a glucose challenge (Figure 1G, H, inset: AUC), in males or females based on genotype. Additionally, we did not observe any significant differences in insulin levels 30 minutes (T30, Supplemental Figure 1C) or 60 minutes (T60, Supplemental Figure 1C) after a glucose challenge in males or females based on genotype.

However, the area under the curve (AUC) from the OGTT shows a trend toward the *Atp10A*$^{-/-}$ female mice having greater glucose excursion compared to *Atp10A*$^{+/+}$ controls. We also found no significant difference in fasting blood glucose and insulin levels between WT and KO females on a normal chow diet (Supplemental Figure 3E,F). Therefore, in contrast to expectations based on prior reports (31,32), *Atp10A* deficiency does not appear to perturb whole-body glucose homeostasis.

*Atp10A deficiency causes diet-induced dyslipidemia in females.* To further probe the influence of *Atp10A* on whole-body metabolism, we measured the concentration of free fatty acids (FFA), cholesterol (chol), and triglycerides (TG) in the mouse plasma. While the male mice showed no difference in plasma lipids based on genotype (Figure 2A-C), the female *Atp10A*$^{-/-}$ mice display substantially elevated plasma concentrations of FFA (Figure 2D), chol (Figure 2E), and TG (Figure 2F) compared to *Atp10A*$^{+/+}$ controls. To further explore this female-specific dyslipidemia phenotype, we performed fast performance liquid chromatography (FPLC) on plasma to assess the relative size and lipid content of the different lipoprotein fractions (Figure 2G). We found that the *Atp10A*$^{-/-}$ mice carry most of their TG and cholesterol in smaller sized very low-density lipoprotein (VLDL) and high-density lipoprotein (HDL) particles, respectively (indicated by a shift to the right in the chromatograms). We also compared the AUC of the VLDL (TG) (Figure 2H) and HDL (cholesterol) (Figure 2I) fractions and found that the *Atp10A*$^{-/-}$ mice trend toward having more lipids in these fractions compared to controls. Together, these results show that *Atp10A* deficiency causes female-specific dyslipidemia and changes to lipoprotein metabolism after HFD feeding.

*Atp10A deficiency in females causes substantial changes to the plasma lipidome and visceral fat transcriptome after HFD.* To get a broader view of the dyslipidemia we observed in the plasma of female *Atp10A*$^{-/-}$ mice, we performed mass spectrometry-based untargeted lipidomics on plasma from female *Atp10A*$^{-/-}$ and *Atp10A*$^{+/+}$ mice after 12 weeks on HFD. We found that

*Atp10A* deficiency resulted in statistically significant changes to the abundance of a large number of plasma lipid species; 591 in total, with 324 of these observed from positive ion mode and 267 from negative ion mode lipidomics (Figure 3A,
Study ID ST002696, http://dx.doi.org/10.21228/M83H7N). To highlight how *Atp10A* deficiency altered specific classes of lipid species, we plotted the log2(Fold Change) of lipid species that were significantly changed and calculated the % of the lipid species in each group that had a positive fold change (increase in abundance, green values) versus a negative fold change (decrease in abundance, blue values) (Figure 3B). Interestingly, we saw modest increases in the abundance of ATP10A's lipid substrates, PC and hexosylceramides (this includes GlcCer and galactosylceramide (GalCer)). Surprisingly, we observed that plasma eicosanoid, bile acid and fatty acid (FA) conjugate species were dramatically depleted in *Atp10A*$^{-/-}$ mice compared to *Atp10A*$^{+/+}$ controls.

We further probed the influence of *Atp10A* on metabolism by performing RNAseq on visceral fat (Figure 3C, NCBI GenBank accession numbers: SRR24233646, SRR24233645). We found that 166 genes were differentially expressed in *Atp10A*$^{-/-}$ compared to *Atp10A*$^{+/+}$ mice, where 29 were downregulated and 137 were upregulated. Some notable differences were substantial increases in expression of *Lipf* and *Pla2g5,* encoding a TG lipase (normally expressed in the stomach) and a secreted phospholipase $A_2$, respectively, in *Atp10A*$^{-/-}$ mice (Figure 3C, Supplemental Table 2). Additionally, the orphan G protein-coupled receptor, GPR50, was upregulated 571-fold and this gene has been linked to circulating TG and HDL levels in humans (37), energy metabolism in mice (38), and the attenuation of inflammation and insulin signaling in 3T3-L1 adipocytes (39).

These studies show that *Atp10A* deficiency results in changes to the abundance of a large number of circulating lipid species as well as expression of mRNA transcripts in visceral fat. Taken together, these results indicate that ATP10A has a substantial role in lipid metabolism in female mice fed a HFD. The potential mechanistic links between the lipid transport activity of

ATP10A and whole-body lipid metabolism are shown in Figure 3D. By translocating PC and GlcCer from the outer leaflet to the inner leaflet of the plasma membrane, ATP10A provides substrates to intracellular lipid metabolism enzymes for production of bioactive lipid signaling molecules while decreasing the availability of PC and GlcCer to molecules in circulation (i.e. lipoproteins, lipases) (Figure 3D). Thus, this flipping could affect levels of PC, GlcCer, and downstream metabolites in the intracellular space and in circulation (Figure 3B) as well as change the expression levels of lipid handling enzymes (Figure 3C).

*Atp10A deficiency results in changes to liver metabolic signaling and lipid handling.* Next, we evaluated potential hepatic mechanisms responsible for the metabolic phenotypes observed in the female mice after HFD, by examining key regulators of energy and lipid metabolism in the liver (Figure 4F). Diacylglycerol acyltransferases (DGATs) catalyze the final step in TG synthesis (Figure 4F) and we found that DGAT2 was significantly elevated in HFD-fed *Atp10A*$^{-/-}$ females (Figure 4A,B). AMP kinase (AMPK) is a central regulator of energy metabolism that inhibits acetyl-CoA carboxylase (ACC) by phosphorylating it at S79; and thus inhibits the lipogenesis pathway (Figure 4F). We showed the liver kinase B1 (LKB1)-dependent stimulatory phosphorylation of AMPK$\alpha$ at T172 and AMPK-dependent inhibitory phosphorylation of ACC at S79 were significantly increased in *Atp10A*$^{-/-}$ females (Figure 4A,C); suggesting downregulation of *de novo* lipogenesis in liver. Indeed, we found that *Atp10A*$^{-/-}$ mice have less liver FFA (Supplemental Figure 5A). Thus, excess TG in *Atp10A*$^{-/-}$ plasma is likely driven by FFA from adipose tissue that is converted to TG and secreted by the liver. We also measured levels of several other liver lipid species and found no changes in total cholesterol, cholesterol esters (CE), unesterified cholesterol, TG, PL, or ceramides based on genotype (Supplemental Figure 5B-G). We did find that there was an increase in the abundance of unsaturated vs. saturated species of several TG and PL species and one CE species (Supplemental Figure 5H, I). Even though the amount of cholesterol and TG in the liver was not different based on genotype, Oil

Red O stained lipid droplets from the *Atp10A*$^{-/-}$ mice were larger on average compared to *Atp10A*$^{+/+}$ (Supplemental Figure 5J-L). Therefore, *Atp10A* deficiency results in changes to the levels and phosphorylation state of several proteins involved in lipid metabolism as well as changes to the amount of and saturation state of several lipid species in the liver.

Next, we probed the phosphorylation state of proteins in the insulin signaling pathway that are upstream of DGAT 1/2, ACC, and AMPK$\alpha$ within the liver (Figure 4F). We found a decrease in the activating phosphorylation of the insulin receptor β subunit (IRβ) at Y1146, insulin receptor substrate-1 (IRS-1) at S612, and Akt at S473/T308. Lastly, we observed a decrease in the Akt-dependent inhibitory phosphorylation at GSK-3B at S9 in *Atp10A*$^{-/-}$ females (Figure 4D,E). Interestingly, we also observed a decrease in the activating phosphorylation of cytosolic phospholipase 2 ($cPLA_2$) at S505 in the *Atp10A*$^{-/-}$ mice (Figure 4D,E). $cPLA_2$ is an enzyme that catalyzes the hydrolysis of PLs, such as PC, to lysoPLs and AA, and this fatty acid species can be oxidized to form eicosanoids. These results are indicative of liver insulin resistance in *Atp10A*$^{-/-}$ mice, as plasma insulin levels did not differ based on genotype (Figure 1F). Altogether, these studies reveal that *Atp10A* deficiency in females fed a HFD results in several alterations to the liver, including in lipid metabolism and handling as well as in insulin signaling.

*ATP10A is expressed in ECs.* Next, we wanted to determine where ATP10A is expressed in mice to better understand the potential mechanisms behind its effects on metabolism. To do this, we produced an anti-ATP10A antibody and tested its specificity in HeLa cells overexpressing an HA-tagged ATP10A (Supplemental Figure 6A, B). ATP10A is large, integral membrane protein that often aggregates when subjected to SDS-PAGE and migrates as a high-molecular weight smear above 250 kDa (Supplemental Figure 6B). We then probed several mouse tissues with the anti-ATP10A antibody via immunoblotting and found a band specific for ATP10A above 250 kD in vas deferens, testes, liver, and visceral fat from *Atp10A*$^{+/+}$ mice, that

was absent in the *Atp10A*$^{-/-}$ tissues (Figure 5A). We did not observe ATP10A via immunoblotting in the heart or brain (Figure 5A), however using immunofluorescence imaging, we observed weak ATP10A staining in the heart that appeared to be in vessels based on morphological assessment (Supplemental Figure 6C). We applied this method to vas deferens samples and observed robust ATP10A-positive staining of most cells in *Atp10A*$^{+/+}$ mice that was not present in the *Atp10A*$^{-/-}$ mice, further confirming the specificity of the anti-ATP10A antibody (Figure 5B). For liver and visceral fat, we observed specific staining for ATP10A that appeared to be in ECs (Figure 5C), but found no specific staining for ATP10A in hepatocytes or adipocytes. To confirm endothelial expression, we used immunohistochemistry to examine CD31, a vascular EC marker, on sequential tissue slides (to examine the same vessels seen via immunofluorescence). We found that cells that were positive for ATP10A staining were also positive for CD31 staining in *Atp10A*$^{+/+}$ liver and visceral fat, and that the ATP10A signal was absent in ECs from *Atp10A*$^{-/-}$ mice (Figure 5C). Next, we detected endogenous expression of ATP10A in human umbilical vein ECs (HUVECs) and ECs from mouse auxiliary lymph nodes (SVEC4-10) via immunoblot analysis (Figure 5D). Note that the ATP10A band migrated just below 150 kD, close to the calculated molecular weight of ATP10A (168 kD), instead of at the top of the gel (Figure 5A), presumably because the decreased complexity of the cell culture lysates, compared to tissues, helped improve solubilization and denaturation of the protein. Additionally, we observed ATP10A staining, primarily at the plasma membrane, via immunofluorescence imaging in both HUVEC and SVEC4-10 (Figure 5E). These experiments show that ATP10A is expressed in mouse vas deferens, testes, ECs in heart, liver and visceral fat, as well as human vascular ECs (HUVECs) and mouse auxiliary lymph nodes ECs (SVEC4-10).

*Atp10A deficiency disrupts insulin signaling pathways in ECs.* We next determined the impact of ATP10A expression on insulin signaling in cultured ECs, HUVEC and SVEC4-10. To do this, we

first used an siRNA approach to knockdown ATP10A and confirmed the reduction of this protein by immunoblot (Supplemental Figure 7A,D HUVEC knockdown: ~50%, SVEC4-10 knockdown: ~70%) and immunofluorescence (Supplemental Figure 7B,E). The ATP10A siRNA-treated or control cells (non-silencing siRNA) were stimulated with insulin and samples were collected over a 60-minute time course (Figure 6A,B, Supplemental Figure 8A,B). The control cells responded with a rapid increase in IRβ activating phosphorylation accompanied by increased activating phosphorylation of IRS-1, Akt and eNOS, as well inhibitory phosphorylation of GSK-3β. Akt directly phosphorylates eNOS on S1177 and GSK-3β on S9, thus confirming the insulin-dependent activation of Akt in these cells. $cPLA_2$ activating phosphorylation, which is downstream of the Ras/ERK arm of this pathway, was also stimulated by insulin. By striking contrast, the ATP10A siRNA-treated cells failed to respond to insulin stimulation and no significant change in phosphorylation was observed for any downstream component of the insulin-dependent pathway. However, we noticed that the level of phosphorylation for each tested protein appeared elevated in the knockdown cells relative to the control cells at time 0, for which no insulin was added. Therefore, we re-examined the time 0 samples from control and knockdown cells side-by-side on the same immunoblot for quantitation (Figure 6C,D, Supplemental figure 7C,F). Indeed, the basal levels of IRβ, IRS-1, Akt and eNOS phosphorylation were elevated two to four-fold in ATP10A siRNA-treated cells. GSK-3β and $cPLA_2$ were also significantly hyperphosphorylated in ATP10A knockdown SVEC4-10 cells but were not significantly different in the HUVECs. Altogether, basal insulin signaling, observed at time 0, in cultured ECs was substantially elevated in ATP10A siRNA-treated cells compared to control.

Next, we sought to determine if basal signaling through Akt is elevated in ECs of the *Atp10A*$^{-/-}$ mouse. To do this, we measured the extent of eNOS phosphorylation by Akt in aorta, a tissue rich in ECs. eNOS is almost exclusively expressed in ECs, therefore p-eNOS$^{S1177}$ levels provide a readout of Akt activity in these cells. We found that *Atp10A*$^{-/-}$ mice exhibit elevated

basal Akt-dependent phosphorylation of eNOS in aorta compared to *Atp10A*$^{+/+}$ mice for both females and males (Females (normal chow fed): Figure 6E,F; Males: Supplemental 8C,D). Taken together, these results reveal a role for ATP10A in regulating insulin signaling in ECs (HUVEC, SVEC4-10, aorta). Decreasing ATP10A expression in ECs results in elevated phosphorylation of proteins in the insulin signaling pathway during basal conditions, which ablates the ability of the cells to respond to insulin stimulus (added insulin).

**Discussion**

This study reveals a requirement for ATP10A in protecting female mice from dyslipidemia and protecting both sexes from endothelial dysfunction. *Atp10A*$^{-/-}$ mice fed a HFD do not gain more weight or exhibit perturbed glucose metabolism compared to controls (Figure 1). Despite the normal weight gain and body composition, female *Atp10A*$^{-/-}$ mice display elevated plasma levels of FFA, cholesterol, and TGs, and these parameters are unchanged in male *Atp10A*$^{-/-}$ mice relative to WT controls (Figure 2). The plasma lipidome and visceral fat transcriptome are also substantially perturbed in the knockout female mice (Figure 3), and basal insulin signaling in the liver is depressed (Figure 4) although the plasma insulin levels are comparable to wild-type littermates (Figure 1F, Supplemental Figure 1C, D). We also show that ATP10A is expressed in ECs (Figure 5). In contrast to the liver insulin signaling *in vivo*, *Atp10A* deficiency in ECs *in vitro* causes hyperactive basal signaling through IRS-1, Akt, $cPLA_2$, and eNOS as well as a failure to respond to insulin stimulation (Figure 6). We also find that Akt-dependent phosphorylation of eNOS is significantly elevated in arteries from female and male mice (Figure 6E,F, Supplemental Figure 8C,D), implying that the same hyperactive signaling occurs in *Atp10A*$^{-/-}$ ECs *in vivo*.

As of yet, we do not know the causal relationship between the dyslipidemia, liver metabolic signaling defects, and endothelial dysfunction characterized by hyperactive insulin

signaling and increased phosphorylation of eNOS caused by *Atp10A* deficiency. However, our findings provoke speculation about ATP10A-regulated interactions between different cell types and their impact on metabolic processes. Based on our ability to detect ATP10A protein in ECs but not in adipocytes or hepatocytes, we hypothesize that dysregulation of IR-dependent signaling within ECs results in insulin resistance in resident hepatocytes and alterations to transcription in visceral fat resident adipocytes (Figure 7A). However, the Mouse Cell Atlas (40) and Liver Cell Atlas (41), public databases with single-cell RNA sequencing data from *Mus musculus,* both report expression of *Atp10A* in liver ECs as well as hepatocytes. Thus, it is also possible that low levels of ATP10A protein expression in hepatocytes and/or adipocytes is sufficient to provide an important cell-autonomous role in regulating lipid metabolism. Analysis of tissue-specific knockout mice will be needed to distinguish these possibilities. If ATP10A is functioning in hepatocytes, our data suggests that its potential function in hepatocytes is distinct from its function in ECs because *Atp10A* deficiency results in a depression of insulin signaling in liver (where hepatocytes are the most abundant cell type) (Figure 4) and hyperactivation of insulin signaling in ECs (Figure 6). We clearly observe a cell-autonomous role for ATP10A in HUVECs and SVEC4-10 ECs in promoting desensitization of the insulin receptor. Therefore, we hypothesize that translocation of substrate lipids by ATP10A modulates the cellular lipid environment and/or the production of bioactive lipids in the cell to facilitate attenuation of the insulin receptor (Figure 7B).

Interestingly, there is an established relationship between insulin resistance, endothelial dysfunction, and dyslipidemia. Indeed, dyslipidemia and insulin resistance are tightly linked (42,43) and eNOS has also been shown to regulate lipid metabolism. *eNOS*$^{-/-}$ mice display liver lipid accumulation (44), hypertension (45), and dyslipidemia characterized by elevated plasma levels of cholesterol, TGs, and FFAs (46). Additionally, insulin resistance originating at the endothelium could result in dyslipidemia via modulation of the expression of lipoprotein lipase

(LPL), an enzyme expressed on the endothelium that degrades circulating TGs, and is regulated by insulin (Figure 7B, 47-50). A reduction in LPL activity can reduce the clearance of TG from the plasma and result in hypertriglyceridemia (51,52). Further research is needed to determine if endothelial dysfunction causes the dyslipidemia and liver insulin resistance in *Atp10A*$^{-/-}$ mice, or if these are independent and separable functions of ATP10A.

The response of ECs to insulin is mediated by IRs and can affect the systemic response to insulin by inducing vasodilation via activation of eNOS, thereby affecting glucose disposal (53,54). Interestingly, a vascular EC-specific deletion of the IR perturbs the kinetics of insulin action on peripheral tissues and accelerates the development of systemic insulin resistance in HFD-fed mice, implying either an important role for the IR in insulin transport across the vascular endothelium or insulin-dependent signaling in ECs (55). Moreover, HFD-induced insulin resistance appears to develop first in the vasculature, accompanied by changes in the production of nitric oxide (NO), before it develops in muscle, liver or adipose tissue (56,57). Therefore, the endothelium itself is a target of insulin and insulin resistance can exist at the level of ECs. These findings support the idea that *Atp10A* deficiency in ECs results in hyperactive signaling at basal levels of insulin first, and hepatic insulin resistance occurs subsequently. A model of excess insulin signaling in ECs resulting in hepatic insulin resistance has been previously described (58). The authors showed that mice carrying an EC-specific knockout of all three FoxO isoforms display hyperactive insulin signaling in ECs and hepatic insulin resistance, which was attributed to excessive eNOS activity and nitrosylation of hepatic IRs. Further studies are needed to determine if hyperphosphorylation of eNOS observed in *Atp10A* deficient ECs (Figure 6E) leads to excess nitrosylation of IRs in underlying tissues. Additionally, the function of ATP10A in ECs could be important for other tissues; ECs and pericytes regulate insulin permeability across the blood-brain barrier (59) and vascular permeability of insulin in the muscle is a major determinant of muscle insulin action (60); therefore, further studies are needed to elucidate if *Atp10A* deficiency results in changes to brain and/or muscle function.

*Atp10A* deficient female mice exhibit dyslipidemia characterized by elevated plasma FFA, cholesterol, TG, and alterations in the size and lipid content of both VLDL and HDL (Figure 2D-G). It is likely that an increased release of FFA from adipose tissue drives an increase in TG synthesis in the liver and its secretion in VLDL (Figure 4F) (61-63). Additionally, dysregulation in adipose tissue could also be responsible for the excess circulating cholesterol (64). Interestingly, we observed an increase in *Lipf* mRNA transcripts in visceral fat from *Atp10A* deficient mice (Figure 3C). *Lipf* codes for a gastric lipase, however it has been shown to be highly expressed in adipose tissue in a mouse model of diet-induced obesity (65). It is possible that *Atp10A* deficiency exacerbates this phenomenon, in the absence of diet-induced obesity, via an unknown mechanism. Another potential source of TGs is *de novo* lipogenesis in the liver; however, *Atp10A* deficient mice exhibit an increase in activating phosphorylation of hepatic AMPK$\alpha$ (Figure 4A,C), a master regulator of lipid metabolism, that increases fatty acid oxidation and decreases *de novo* lipogenesis (66), as well as decreased total liver FFAs (Supplemental Figure 5A). Thus, it is unlikely that FA production in the liver is driving the excess plasma TG. Mice naturally lack the cholesterol ester transfer protein (CETP) and have increased cholesterol in HDL relative to humans. As expected, *Atp10A* deficient mice carry most of their circulating cholesterol in HDL; but unexpectedly, this cholesterol is mostly carried in smaller HDL particles compared to controls. This observation may suggest a potential issue with the quality of HDL in these mice (67). Additionally, *Atp10A* deficient mice show reduced circulating levels of bile acids (Figure 3A,B), which are important signaling lipids with implications in cholesterol metabolism and cardiovascular health (68). Further research is needed to understand the mechanisms underlying dyslipidemia observed in *Atp10A* deficient mice and if this defect is caused by endothelial dysfunction.

The molecular basis for the female-specific dyslipidemia we observe in *Atp10A*$^{-/-}$ mice is unclear. There are established differences in disease severity and prevalence between men and women (69). Premenopausal women tend to have lower cardiovascular risks compared to men

which could be due to the effects that estrogen exerts on the endothelium (70). The *Atp10A* promoter is predicted to have a transcription factor binding site for estrogen receptor alpha (Genecards.org, QIAGEN), so it is possible that differences in expression due to sex contribute to the consequences of *Atp10A* deletion. However, the effect of sex and diet on the phenotypes caused by *Atp10A* deficiency in ECs is not apparent because we observe similar signaling perturbations in HUVECs, cells from male and/or female humans, SVEC4-10 cells from male mice, and aorta from female (normal chow fed) and male mice (Figure 6E,F, Supplemental Figure 8C,D). Thus, endothelial dysfunction in *Atp10A* deficient mice occurs in both sexes, independent of diet, however, the dyslipidemia is female-specific, suggesting that this phenotype is either promoted by estrogen in females or suppressed by testosterone in males. Additionally, we did not measure the lipoprotein profiles, perform plasma lipidomics, or measure metabolic liver signaling pathways in male mice because they did not exhibit diet-induced dyslipidemia (Figure 2A-C). It will be interesting to examine these metabolic and lipid profiles in male and female mice fed different diets to fully elucidate the effect of sex and diet on the observed phenotypes.

The hyperactive signaling in ATP10A knockdown ECs appears to originate at the level of the IR; however, due to a lack of antibodies that can distinguish between phosphorylated IR and IGF1R, the p-IRβ labeled in our western blots could also represent p-IGF1R (Figure 6, Supplemental Figure 7&8). This is a common problem given the high homology between IR and IGF1R. Therefore, the specific receptor(s) responsible for the hyperactive basal signaling observed in ATP10A knockdown ECs is still an open question. We have focused our studies on the IR, but it is also possible that other receptor tyrosine kinases that activate the PI3K/Akt and Ras/MAPK pathways are also hyperactivated in ATP10A-deficient ECs. Additionally, HUVECs and ECs in mouse aorta are macrovascular cells, and we have not studied the influence of ATP10A on microvessels. This is an important distinction to make because macrovessels and

microvessels exhibit distinct characteristics and respond to stimuli differently; indeed, eNOS has been shown to mediate differential effects in macro- and microvessels (71). We observed similar, but distinct, signaling defects in ATP10A knockdown HUVECs and SVEC4-10, mouse lymphatic ECs. Upon knockdown of ATP10A, both cell types exhibited insulin resistance characterized by hyperactive basal signaling; however, unlike in HUVECs, SVEC4-10 displayed a significant increase in activating phosphorylation of GSK3-$\beta$ and $cPLA_2$ at basal insulin levels (Figure 6C,D). Therefore, ATP10A could have distinct effects in lymphatic vascular ECs compared to blood vascular ECs and this also requires further study.

Our studies indicate that *Atp10A* deficiency disrupts the regulation of $cPLA_2$ activity and the production of eicosanoids, which could further exacerbate endothelial dysfunction. We found a reduction of activating phosphorylation of $cPLA_2$ in the liver and an increase in ECs (Figure 4D,E, Figure 6) as well as a depletion of circulating levels of eicosanoids (Figure 3A,B) due to ATP10A deficiency. $cPLA_2$ can hydrolyze PC to release AA which can be oxidized to form eicosanoids, bioactive lipids with roles in inflammation and vasculature maintenance (72,73). $cPLA_2$ can only act on lipids in the cytosolic leaflet and ATP10A could potentially provide additional PC substrate to this enzyme, derived from the extracellular leaflet or an external source, such as lipoproteins. We hypothesize that ATP10A can regulate $cPLA_2$ activity by modulating signaling pathways that activate $cPLA_2$ (Figure 7A) as well as by increasing substrate availability in ECs (Figure 7B). Interestingly, ATP10A can also translocate GlcCer to potentially promote synthesis of ceramide 1-phosphate (C1P), another activator of $cPLA_2$ (74) (Figure 7B). $cPLA_2$ hydrolysis of PC also produces lysoPC, a bioactive lipid that may link saturated FAs to insulin resistance (75). Despite the reduction of eicosanoids in the plasma, there was no substantial difference in the levels of circulating lysoPC based on genotype. It is possible that the increased expression of *Pla2g5* (Figure 3C), a secreted phospholipase, may have compensated for the perturbations in $cPLA_2$ signaling and normalized lysoPC levels in the plasma. Altogether, the modulation of $cPLA_2$ activity due to *Atp10A* deficiency could alter the

levels of vasoactive compounds, and further work is needed to better define the specific influence of ATP10A on eicosanoid production.

Prior studies analyzing mice with an overlapping series of radiation-induced deletions encompassing the *p* locus on chromosome 7 implicated *Atp10A* deficiency in diet-induced obesity, insulin resistance indicated by reduced efficacy of insulin in mediating glucose disposal, and hyperlipidemia (31,32). These phenotypes were observed in heterozygous mice that inherited the chromosomal deletion maternally, suggesting that the paternal *Atp10A* allele was silenced. However, we found no evidence for obesity or metabolic defects in *Atp10A*$^{+/-}$ heterozygous mice inheriting the KO allele paternally or maternally (Supplemental Figure 4), nor did the *Atp10A*$^{-/-}$ homozygous mice display diet-induced obesity or defects in glucose metabolism (Figure 1). These results are in contrast to previous reports, most likely because the mice used in those studies had a large chromosomal deletion that, in addition to *Atp10A*, removed several other genes, some of which are known to be imprinted (76). It is also possible that differences in the strain background or rearing environment alter the susceptibility of *Atp10A*$^{-/-}$ mice to diet-induced obesity and glucose metabolism perturbations. The phenotypes in common between the two *Atp10A* deficient models are the elevated circulating levels of FFAs, cholesterol, and TGs, and the stronger influence of ATP10A on metabolism in female mice relative to males. We have shown that ATP10A promotes endothelial insulin sensitivity and lipid homeostasis. Therefore, a therapeutic that acts as an ATP10A agonist could help treat diseases that disrupt insulin signaling in ECs and/or cause dyslipidemia.

## Methods

*Animals.* All mouse experiments were approved under the Vanderbilt University Institutional Animal Care and Use Committee. Mice were housed in 12 h light/dark cycles in temperature and humidity-controlled facilities with ad-libitum access to diet and water.

*Creating the mouse model.* The *Atp10A* mouse model (knockout allele name: *Atp10Aem1(Vtrg)* (allele designation approval pending)) was created via CRISPR-Cas9 in collaboration with the Vanderbilt Genome Editing Resource. Guide RNAs (crRNA) were created to target *Atp10A* on chromosome 7: Target Intron 1-2: TGACTGCTTAATGATTCGAGG, GAGTGACTGCTAATGATCG, Target Intron 2-3: GGAAAAAGCCCAATTCCACAC, AGCCCAATCCACACAGGAAC. CRISPR editing reagents were delivered into the pronuclei of one-cell fertilized mouse zygotes (C57BL/6J). Approximately 608 bp were deleted using this method: nucleotides 58389679-58390287 (NCBI reference sequence: NC_000073). The resulting pups were biopsied and screened by PCR and Sanger sequencing. The predicted founders were bred to WT C57BL/6J animals and the offspring were genotyped (N1 generation). The offspring with the appropriate genotype were then backcrossed two more times.

*Genotyping.* Mice were genotyped using tail DNA. *Atp10A* DNA products were detected via a multiplexed PCR (Lucigen EconoTaq PLUS GREEN,Biosearch Technologies) followed by gel electrophoresis; *Atp10A-F* (GTGCACTGTATTTGTCTGCC), *Atp10A-R1* *(*CAAAGTCGCCCACTCGGATTTC), *Atp10A-R2* (CCAACCTACGTAAGAACAGG).

*Body composition, body length, and tissue mass.* WT and experimental mice were fed standard chow or 60% HFD (D12492, Research Diets) ad libitum, starting at the age of 3-12 weeks old (see Supplemental Table 1). Mice were weighed once per week to measure body weight gain over time. On the 12$^{th}$ week on the HFD, body composition was assessed via NMR (LF50 Body Composition Mice Analyzer, Bruker, stock # E140000501). Mice were sacrificed with $CO_2$, the body lengths were measured and the mass of the wet tissue was measured using an analytical scale. Tissues were collected and flesh frozen when mice were sacrificed.

*Oral glucose tolerance tests* (OGTT) *and fasting blood glucose/insulin measurements.* Mice were fasted for 5 hours (7AM-12PM) and then an OGTT was performed. Mice were gavaged with 20% w/v dextrose (final 2g/kg body weight), and a tail-vein blood glucose was measured via a glucometer (Accu-Chek, Accu-Chek Aviva Plus Meter) at baseline, 15, 30, 45, 60, 90, and 120 min. The area under of the curve for glucose was calculated using GraphPad Prism. Plasma samples were collected from 5-hr fasted mice via a retroorbital bleed and were used for the insulin assay. Plasma insulin was measured using the Crystal Chem Ultrasensitive Mouse Insulin ELISA Kit (catalog # 90080).

*Plasma lipid and lipoprotein analysis.* Plasma was collected, via a retroorbital bleed or cardiac puncture, from 5-hr fasted mice and 5-hr fasted mice that had undergone an OGTT (see Supplemental Table 1). For males and a portion of the female samples: plasma TG and cholesterol were measured using colorimetric kits (Inifinity, Thermo Scientific, TG catalog #TR22421, chol catalog #TR13421) and plasma FFAs were measured using Abcam's Free Fatty Acid Assay Kit-Quantification (ab65341). For the rest of the females: plasma samples were measured by the Vanderbilt Hormone Assay and Analytical Services Core, where plasma cholesterol and TG were measured by standard enzymatic assays, and plasma FFAs were analyzed with an enzymatic kit (Fujifilm Healthcare Solutions, catalog #999-34691). Lipoproteins were separated using FPLC on a Superose6 column (GE Healthcare) from 150 µl plasma (single mouse or pooled) and the TG and cholesterol content were measured using colorimetric kits (Inifinity, Thermo Scientific, TG catalog #TR22421, chol catalog #TR13421). AUC was calculated using GraphPad Prism.

*Plasma lipidomics.* Plasma was collected, via a retroorbital bleed or cardiac puncture, from 5-hr fasted mice and some samples are pooled plasma (see Supplemental Table 1). Lipid metabolites were extracted from 100 µL plasma by methyl methyltert-butyl ether (MTBE) extraction. The lipid metabolites were then analyzed by HPLC-IM-MS/MS on an Agilent 6560

mass spectrometer using a ZORBAX Extend-C18 RPLC column (Phase A: 0.1% formic acid and 10 mM $NH_4CHOO$ in water, Phase B: 0.1% formic acid and 10 mM $NH_4CHOO$ in 60:36:4 isopropanol:acetonitrile: $H_2O$) (77). Data alignment and biostatical analysis was performed using Progenesis QI (Waters). Tentative compound identifications were assigned using accurate mass databases and a previously described ion mobility-based filtering method (78).

*RNA Sequencing.* Visceral fat was flash frozen in liquid nitrogen and then kept at -80$^{o}$C until thawed at -20$^{o}$C in RNA*later* (ThermoFisher, catalog # AM7030). The tissue was then homogenized in QIAzol Lysis Reagent (Qiagen, catalog #79306) using a Bullet Blender (Next Advance, BT24M). The RNA layer acquired after the QIAzol Lysis protocol was cleaned up using the RNeasy Lipid Tissue Mini Kit (Qiagen, catalog #NC9036170). Quality control measurements and Next Generation Sequencing (NGS) was performed on 20 uL of RNA (>10 ng) by Vanderbilt Technologies for Advanced Genomics (VANTAGE); briefly, NEBNext Ultra II Directional RNA kit (Cat no: E7760L) was used and for the sequencing; NovaSeq 6000 and PE150 read lengths were used.Analysis of NGS data was performed by Vanderbilt Technologies for Advanced Genomics Analysis and Research Design (VANGARD).

*Cell cultures and treatment.* Human Umbilical Vein Endothelial Cells (HUVEC) were from Lonza (Walkersville, MD; cat. #C2519A, lot #21TL347550) and were cultured in EGM$^{TM}$-2 medium (Lonza, Walkersville, MD) at 37 $^{o}$C with 5% $CO_2$. SVEC4-10 cells from mouse lymph node endothelium were purchased from ATCC (Manassas, VA) and maintained in DMEM with 10% FBS and 1% penicillin/streptomycin (Life Technologies, Gaithersburg, MD). Cells from passage 2 to 9 were used in this study. For silencing experiments, cells were transfected for 48 h with non-silencing siRNA (50 nM, transfection control) or ATP10A siRNA (combined 25 nM each ATP10A sequences #1 and #2) using Lipofectamine RNAiMAX (Invitrogen by Thermo Fisher Scientific) according to manufacturer's instructions. Silencer Select pre-designed ATP10A

siRNAs (human sequence #1 (5'-3'): CAACGACCUGAGUAGGUUUtt; human sequence #2 (5'-3'): CCAAUUUCCUUAUACGUUUtt; mouse sequence #1 (5'-3'): CCUUAUAUGUUUCCAUUGAtt; mouse sequence #2 (5'-3'): CAAUGACCUGAGUAGGUUUtt) and Silencer Select Negative control #1 siRNA were bought from Ambion by Life Technologies™. For treatment with insulin, human recombinant zinc solution of insulin was used (Gibco™ by Thermo Fisher Scientific). Cells were treated with either growth medium (control) or with 100 nM insulin (diluted in growth medium) for 0-60 min.

*Immunoblot analysis.* HUVEC or SVEC4-10 were harvested at the indicated times of respective treatment. Total protein extraction was performed using M-PER (Pierce, Rockford, IL) with phosphatase and protease inhibitors (Sigma). For tissue samples, T-PER (Pierce, Rockford, IL) with phosphatase and protease inhibitors (Sigma) were used. Protein concentration was quantified using BCA Reagent (Pierce, Rockford, IL). Protein extracts (40 µg for cells; 100 µg for tissues) were subjected to Western immunoblot analysis. The following primary antibodies were used for detection of: ATP10A (Vanderbilt Antibody and Protein Resource, Vanderbilt University, see below), DGAT1 (sc-32861, Santa Cruz Biotech), DGAT2 (sc-66859, Santa Cruz Biotech), phospho-AMPKα$^{T172}$ (#2535, Cell Signaling), AMPKα (#2532, Cell Signaling), phospho-ACC$^{S79}$ (#3661, Cell Signaling), ACC (#3676, Cell Signaling) , phospho- IGF-IRβ$^{Y1131}$/IRβ$^{Y1146}$ (#3021, Cell Signaling), phospho-IGF-IRβ$^{Y1135/1136}$/IRβ$^{Y1150/1151}$(#3024, Cell Signaling), IRβ (#3025, Cell Signaling), phospho-IRS-1$^{S612}$ (#3203, Cell Signaling), IRS-1 (#3407, Cell Signaling), phospho-Akt$^{T308/S473}$ (#13038/#4060, Cell Signaling), Akt (#9272, Cell signaling), phospho-GSK-3β$^{S9}$ (#5558, Cell Signaling), GSK-3β (#9315, Cell Signaling), phospho-cPLA$_2$α$^{S505}$(#53044, Cell Signaling), cPLA$_2$α (#5249, Cell Signaling), phospho-eNOS$^{S1177}$ (ab215717, Abcam), eNOS (#32027, Cell signaling). Antibody to actin (#4970, Cell Signaling) was used to evaluate protein loading in each lane. Immunoblots were developed using the Western Lightning Chemiluminescence Plus detection system (PerkinElmer,

Wellesley, MA) according to the manufacturer's protocol. Intensity of the immunoblot bands was measured using AI600 CCD Imager for chemiluminescent assays (Amersham). Densitometry was performed using ImageJ. For quantification, OD of bands for phosphoprotein was normalized to total protein and β-actin; otherwise, OD of bands for total protein was normalized to β-actin.

*Generation of ATP10A antibodies.* Anti-ATP10A antibody were produced by Vanderbilt Antibody and Protein Resource. ATP10A peptides 1 (27 RTRTVRSNLLPPC 38), 3 (498 HKTQSIKSHRRTC 510) and 5 (1280 QTLLGDPLFYLTC 1292) for antibody production were chosen based on conservation between mouse and human ATP10A orthologs, lack of conservation with ATP10B and ATP10D paralogs, and predicted water solubility (https://pepcalc.com) (Supplemental Figure 6A). Peptide epitopes were synthesized (GenScript, USA, Inc.) with a C-terminal Cys residue and conjugated to Imject™ Maleimide-Activated mcKLH, Imject™ Maleimide-Activated BSA, and SulfoLink™ Coupling Resin following the manufacturer's recommended protocol (ThermoFisher Scientific) by the Vanderbilt Antibody and Protein Resource (VAPR) group. The three peptide-Keyhole Limpet Hemocyanin (KLH) conjugates were used for antibody production in a single rabbit (VU579, Cocalico, Stevens, PA). Antibodies recognizing the peptide epitopes were purified from the rabbit by differential affinity chromatography using the peptide conjugated resin. Briefly, 5 ml of antisera was passed over the peptide 1 column (2 ml) and the material that failed to bind was then applied sequentially to the peptide 3 and 5 columns. After washing with 40-50 ml PBS, bound antibodies were eluted from each column with 8.5 ml of 100 mM glycine, pH 2.5 and collected in tubes containing 1.5 M Tris-HCl, pH 8. Finally, to ensure peptide specificity, antibodies eluted from one peptide column were applied sequentially to the other two columns and the flow-through was retained. Affinity purifications were performed in duplicate to generate anti-peptide 1A and 1B, anti-peptide 3A and 3B, and antipeptide 5A and 5B antibodies. The specificity of the affinity purified antibodies

was then assessed by dot blot analysis using the peptide-BSA conjugates. The rabbit produced antibodies to all three peptides but only anti-peptide 1 recognized full-length ATP10A (Supplementary Figure 6B).

*Immunofluorescent staining of mouse tissues.* Tissue was fixed in 10% neutral buffered formalin and further processing and paraffin embedding was done by the Vanderbilt Translation Pathology Shared Resource (TPSR). Tissue sections are 5 μm thick. To stain paraffin embedded sections, the sections underwent re-hydration, antigen retrieval, blocking, and antibody treatment (79). The slides were treated with anti-ATP10A (1:20) followed by goat anti-rabbit Alexa-Fluor 647 secondary antibody (1:1,000, Abcam, #150083) and ProLong Gold Antifade Mountant with DAPI (Thermo Fisher, catalog # P36931). Images of tissues were acquired using a confocal microscope (Zeiss LSM 880 with AiryScan) with a Zeiss C Plan Apochromat ×40/1.40 Plan-Apochromat Oil using the ZEN black software. Confocal images were taken of vas deferens, liver, visceral fat, and heart. Laser irradiation at 633 nm was used to excite the Alexa-Fluor 647, and at 405 nm to excite DAPI. Detector gain and laser intensity were constant for all experimental groups. Images were false colored green and edited using ImageJ (images from the same tissues were edited using the same scripts).

*Immunofluorescent staining of cells.* Routinely grown HUVEC or SVEC4-10 cells were plated on Nunc™ Lab-Tek™ Chamber Slides (Thermo Fisher Scientific, #177399). For silencing experiments, cells were transfected for 48 h with non-silencing or ATP10A siRNA as described previously. Cells were fixed, washed, permeabilized, blocked and treated with anti-ATP10A antibody (1:20) followed by goat anti-rabbit Alexa-Fluor 488 secondary antibody (1:1,000, Invitrogen by Thermo Fisher Scientific, #A11008) and ProLong Gold Antifade Mountant with DAPI. Images of cells were acquired using a confocal microscope (Zeiss LSM 880 with AiryScan) with a Zeiss C Plan Apochromat ×63/1.40 Plan-Apochromat Oil using the ZEN black software. Laser irradiation at 488 nm was used to excite the Alexa-Fluor 488, and at 405 nm to

excite DAPI. Detector gain and laser intensity were constant for all experimental groups. Images were edited using ImageJ (images from experimental groups were edited via the exact same parameters).

*Immunohistochemistry (Tissues).* Tissue was fixed in 10% neutral buffered formalin and further processing and paraffin embedding was done by the Vanderbilt Translation Pathology Shared Resource (TPSR). Tissue sections are 5 μm thick. Slides were placed on the Leica Bond Max IHC stainer. All steps besides dehydration, clearing and cover slipping are performed on the Bond Max. Slides are deparaffinized. Heat induced antigen retrieval was performed on the Bond Max using their Epitope Retrieval 2 solution for 20 minutes. Slides were incubated with anti-CD31 (Dianova, catalog # DIA-310) for one hour at a 1:75 dilution and followed by a biotinylated anti-rat (Vector Laboratories, Inc., Burlingame, catalog # BA-4000) for 15 minutes at a 1:2000 dilution. The Bond Refine (catalog # DS9800) detection system was used for visualization. Slides were then dehydrated, cleared and cover slipped. Images of tissues were acquired using light microscopy (Zeiss AxioPlan, Upright Fluorescence Microscope, Germany) with a x63/1.0 Oil using the Zeiss Axio Color Camera (Axiocam 208c) and the ZEN 3.1 software (blue edition). Microscope settings were held constant for all experimental groups.

*Promethion System.* Indirect calorimetry and additional measures of food intake and physical activity were performed in open-circuit indirect calorimetry cages (Promethion System, Sable Systems International) at Vanderbilt Mouse Metabolic Phenotyping Center (MMPC). One week prior to the experiment start date, mice were singly housed for acclimation. On the day of the experiment start date, mice were weighed and body composition was assessed. The mice were placed in the cages of the Promethion system, one mouse per cage. The cages were housed in a light and temperature-controlled chamber. The light cycle was set on a 12:12h cycle (6am-6pm). Mice were left undisturbed for 5 days during which all the measurements were made. The system periodically measured rates of O2 consumption (VO2) and CO2 production (VCO2) for

each cage, as well as food intake and physical activity (infrared beam array). Data were processed in time segments (daily 24-hour, and 12-hour dark/12-hour light), and averages calculated for each as well as for the 24-hour period. After 5 days, the mice were removed from the cages, and body composition and weight were measured again.

*Measuring liver lipids.* Liver FFA, total cholesterol, cholesterol ester, unesterified cholesterol, TG, PLs, and ceramides were measured by the Vanderbilt Hormone Assay and Analytical Services Core using methods described in (80, 81).

*Oil Red O.* Livers were placed in frozen section medium (Epredia, Neg-50, catalog #22-110-617) and then placed on dry ice. When the frozen section medium was solidified, the livers were placed at -20$^{o}$C until further processing. Further processing was done by the Vanderbilt Translation Pathology Shared Resource (TPSR): Slides were brought to room temperature and placed in 10% NBF solution for 10 minutes. The Newcomer Supply Tech Oil Red O, Propylene Glycol staining kit (Newcomer Supply, catalog # 12772B) was used for visualization. Slides were then cover slipped with aqueous mounting medium. In regard to Oil Red O scoring: Dr. Katherine Gibson Corley, a board-certified veterinary pathologist at the Vanderbilt TPSR, created the scoring system used to score the Oil Red O stained liver sections. The scoring system is characterized by: 0= no Oil Red O staining, 1=rare and scattered Oil Red O staining, 2=multi-focal and coalescing Oil Red O staining, 3=diffuse Oil Red O staining (in whole tissue). To score the slides, the scorer was blinded to the slide IDs and then scored the slides twice, on two separate days. Then the scores from both days were compared and if they did not match, the scorer viewed the slide again and decided on a final score. The diameter of the Oil Red O positive lipid droplets was measured from slides with a score of 2, using ImageJ.

*Statistics.* All statistical analysis was done using GraphPad Prism, version 9.5.0 (GraphPad Software). Error bars indicate mean with standard error of the mean (SEM). When more than 2

groups were compared, a 2-way ANOVA was used with Dunnett's correction for multiple comparisons with a control group. Šidák's correction was used for comparison of groups of means. Differences between group mean values were tested using a 2-tailed Student's *t* test or a Mann-Whitney *U* test for nonparametric data. A *P* value of less than 0.05 was considered statistically significant.

*Study approval.* The animal protocol was approved by Vanderbilt University Medical Center and IACUC.

*Data Availability.* The untargeted lipidomics data is available at the NIH Common Fund's National Metabolomics Data Repository (NMDR) website, the Metabolomics Workbench (82), where it has been assigned Study ID ST002696. The data can be accessed directly via its ProjectDOI: http://dx.doi.org/10.21228/M83H7N.The reads from the RNASeq data can be found at NCBI (https://www.ncbi.nlm.nih.gov/genbank/samplerecord/) using these accession numbers: SRR24233646 (*Atp10A* WT reads) and SRR24233645 (*Atp10A* KO reads).

**Author contributions**

ACN is the first author on this publication; she designed and conducted all of the mouse experiments, collected the tissues analyzed in the paper, and did the microscopy work. Additionally, she created the figures and schematics and wrote the manuscript. EMY conducted all of the western blot experiments and cell culture work, helped create the manuscript figures, and edited the manuscript. LZ helped with the mouse work, tissue collection, and provided intellectual support. BSR conducted the mass spectrometry analysis and analyzed the results. JCM developed the multidimensional mass spectrometry methods and assisted with the lipidomics informatics work. AM helped collect and weigh mouse tissues and tested the specificity of the ATP10A antibody in HeLa cells. KGC created the Oil Red O scoring system.

JAM, JMS and TRG provided funding acquisition, resources, conceptualization, and project administration.

**Acknowledgements**

The authors thank the **Vanderbilt Genome Editing Resource** for creating the *Atp10A* mouse lines and assisting with genotyping (supported by the Cancer Center Support Grant (CA68485), the Vanderbilt Diabetes Research and Training Center (DK020593) and the Center for Stem Cell Biology), the **Vanderbilt Division of Animal Care** veterinarians and technicians for their support with mouse husbandry, the **Vanderbilt Metabolic Mouse Phenotyping Center (MMPC)** especially Louise Lantier, for providing the NMR machine for body composition measurements and for performing the indirect calorimetry (DK135073, DK020593, S10RR028101), the **Vanderbilt Analytical services core** for measuring plasma and liver lipids (supported by *NIH grant DK020593 (DRTC))*, the **Translational Pathology Shared Resource (TPSR)** for producing all of the paraffin embedded tissue sections and performing the Oil Red O and CD31 staining (supported by NCI/NIH Cancer Center Support Grant P30CA068485), the **Vanderbilt Cell Imaging Shared Resource (CISR)** for providing the Zeiss LSM880 Airyscan Confocal Microscope used in this study (supported *by NIH grants CA68485, DK20593, DK58404, DK59637, and EY08126;* Zeiss LSM880 Airyscan Confocal Microscope *acquired through NIH* 1 S10 OD021630 1), Brian Wadzinski and Ben Spiller in the **Vanderbilt Antibody and Protein Resource** for ATP10A antibody design, production, purification, and testing (supported by the Vanderbilt Institute of Chemical Biology and the Vanderbilt Ingram Cancer Center (P30 CA68485)), the **Center for Innovative Technology at Vanderbilt** for providing access to the mass spectrometry instrumentation and lipidomics software, **The Metabolomics Workbench** *(supported by NIH grants U2C-DK119886 and OT2-OD030544),* Sophia Yu, Teri Stevenson, and Staci Bordash for help with mouse experiments, Joey Lu for help with growing cells, and Bridget Litts for help with finding materials and using equipment. We also thank David Wasserman, Owen McGuiness and David Harrison

for helpful discussions. This work was supported by NIH 1R35GM144123 (to TRG), K01AG077038 (to LZ), NIH R01DK109102, R01HL144846, and T35DK7383, The Department of Veterans Affairs BX002223 (to JMS).

**Conflict of Interests**

The authors have declared that no conflict of interest exists.

Address correspondence to: Todd R. Graham, Department of Biological Sciences, Vanderbilt University, 465 21st Ave S, Nashville, Tennessee 37212, USA. Phone: 615.343.1835; Email: tr.graham@vanderbilt.edu

**References**

1.Aguilar, M., Bhuket, T., Torres, S., Liu, B., & Wong, R. J. (2015). Prevalence of the metabolic syndrome in the United States, 2003-2012. JAMA, 313(19). https://doi.org/10.1001/jama.2015.4260

2. O'Neill, S., & O'Driscoll, L. (2015). Metabolic syndrome: A closer look at the growing epidemic and its associated pathologies. Obesity Reviews, 16(1).https://doi.org/10.1111/obr.12229

3. Fahed, G., Aoun, L., Zerdan, M. B., Allam, S., Zerdan, M. B., Bouferraa, Y., & Assi, H. I. (2022). Metabolic Syndrome: Updates on Pathophysiology and Management in 2021. International Journal of Molecular Sciences, Vol. 23. https://doi.org/10.3390/ijms23020786

4. Rajendran, P., Rengarajan, T., Thangavel, J., Nishigaki, Y., Sakthisekaran, D., Sethi, G., & Nishigaki, I. (2013). The vascular endothelium and human diseases. International Journal of Biological Sciences, Vol. 9. https://doi.org/10.7150/ijbs.7502

5. Tran, V., De Silva, T. M., Sobey, C. G., Lim, K., Drummond, G. R., Vinh, A., & Jelinic, M. (2020). The Vascular Consequences of Metabolic Syndrome: Rodent Models, Endothelial

Dysfunction, and Current Therapies. Frontiers in Pharmacology, Vol. 11. https://doi.org/10.3389/fphar.2020.00148

6. Graupera, M., & Claret, M. (2018). Endothelial Cells: New Players in Obesity and Related Metabolic Disorders. Trends in Endocrinology and Metabolism, Vol. 29. https://doi.org/10.1016/j.tem.2018.09.003

7. Irvin, M. R., Wineinger, N. E., Rice, T. K., Pajewski, N. M., Kabagambe, E. K., Gu, C. C., … Almanzar, N., Antony, J., Baghel, A. S., Bakerman, I., Bansal, I., Barres, B. A., … Zou, J. (2020). A single-cell transcriptomic atlas characterizes ageing tissues in the mouse. *Nature*, *583*(7817). https://doi.org/10.1038/s41586-020-2496-1

8. Arnett, D. K. (2011). Genome-wide detection of allele specific copy number variation associated with insulin resistance in african americans from the hyperGEN study. PLoS ONE. https://doi.org/10.1371/journal.pone.0024052

9. Kengia, J. T., Ko, K. C., Ikeda, S., Hiraishi, A., Mieno-Naka, M., Arai, T., … Sawabe, M. (2013). A gene variant in the Atp10d gene associates with atherosclerotic indices in Japanese elderly population. *Atherosclerosis*, *231*(1). https://doi.org/10.1016/j.atherosclerosis.2013.08.034

10. Andersen, J. P., Vestergaard, A. L., Mikkelsen, S. A., Mogensen, L. S., Chalat, M., & Molday, R. S. (2016). P4-ATPases as phospholipid flippases-structure, function, and enigmas. Frontiers in Physiology. https://doi.org/10.3389/fphys.2016.00275

11.Segawa, K., Kurata, S., Yanagihashi, Y., Brummelkamp, T. R., Matsuda, F., & Nagata, S. (2014). Caspase-mediated cleavage of phospholipid flippase for apoptotic phosphatidylserine exposure. Science. https://doi.org/10.1126/science.1252809

12. Kook, S., Wang, P., Meng, S., Jetter, C. S., Sucre, J. M. S., Benjamin, J. T., … Guttentag, S. H. (2021). AP-3-dependent targeting of flippase ATP8A1 to lamellar bodies suppresses activation of YAP in alveolar epithelial type 2 cells. Proceedings of the National Academy of Sciences of the United States of America, 118(20). https://doi.org/10.1073/pnas.2025208118

13. Ristovski, M., Farhat, D., Bancud, S. E. M., & Lee, J. Y. (2021). Lipid transporters beam signals from cell membranes. Membranes, Vol. 11. https://doi.org/10.3390/membranes11080562

14. van der Mark, V. A., Oude Elferink, R. P. J., & Paulusma, C. C. (2013). P4 ATPases: Flippases in health and disease. International Journal of Molecular Sciences. https://doi.org/10.3390/ijms14047897

15.Naito, T., Takatsu, H., Miyano, R., Takada, N., Nakayama, K., & Shin, H. W. (2015). Phospholipid flippase ATP10A translocates phosphatidylcholine and is involved in plasma membrane dynamics. Journal of Biological Chemistry, 290(24). https://doi.org/10.1074/jbc.M115.655191

16. Roland, B. P., Naito, T., Best, J. T., Arnaiz-Yépez, C., Takatsu, H., Yu, R. J., … Graham, T. R. (2019). Yeast and human P4-ATPases transport glycosphingolipids using conserved structural motifs. Journal of Biological Chemistry. https://doi.org/10.1074/jbc.RA118.005876

17. Francisco Ramos-Martín, Nicola D'Amelio (2022). Biomembrane lipids: When physics and chemistry join to shape biological activity. Biochimie,Volume 203,Pages 118-138,ISSN 0300-9084.https://doi.org/10.1016/j.biochi.2022.07.011.

18. Testerink, N., van der Sanden, M. H. M., Houweling, M., Helms, J. B., & Vaandrager, A. B. (2009). Depletion of phosphatidylcholine affects endoplasmic reticulum morphology and protein traffic at the Golgi complex. Journal of Lipid Research, 50(11). https://doi.org/10.1194/jlr.M800660-JLR200

19.Law, S. H., Chan, M. L., Marathe, G. K., Parveen, F., Chen, C. H., & Ke, L. Y. (2019). An updated review of lysophosphatidylcholine metabolism in human diseases. International Journal of Molecular Sciences, Vol. 20. https://doi.org/10.3390/ijms20051149

20. Knuplez, E., & Marsche, G. (2020). An updated review of pro-and anti-inflammatory properties of plasma lysophosphatidylcholines in the vascular system. International Journal of Molecular Sciences, Vol. 21. https://doi.org/10.3390/ijms21124501

21. Liu, P., Zhu, W., Chen, C., Yan, B., Zhu, L., Chen, X., & Peng, C. (2020). The mechanisms of lysophosphatidylcholine in the development of diseases. Life Sciences, Vol. 247. https://doi.org/10.1016/j.lfs.2020.117443

22. Yamaguchi A, Botta E, Holinstat M. Eicosanoids in inflammation in the blood and the vessel. *Front Pharmacol*. 2022;13:997403. Published 2022 Sep 27. doi:10.3389/fphar.2022.997403

23. Mitchell, J. A., & Kirkby, N. S. (2019). Eicosanoids, prostacyclin and cyclooxygenase in the cardiovascular system. British Journal of Pharmacology, Vol. 176. https://doi.org/10.1111/bph.14167

24. Ishibashi, Y., Kohyama-Koganeya, A., & Hirabayashi, Y. (2013). New insights on glucosylated lipids: Metabolism and functions. Biochimica et Biophysica Acta - Molecular and Cell Biology of Lipids, Vol. 1831. https://doi.org/10.1016/j.bbalip.2013.06.001

25. Mobarak, E., Håversen, L., Manna, M., Rutberg, M., Levin, M., Perkins, R., … Borén, J. (2018). Glucosylceramide modifies the LPS-induced inflammatory response in macrophages and the orientation of the LPS/TLR4 complex in silico. Scientific Reports, 8(1). https://doi.org/10.1038/s41598-018-31926-0

26. Aerts, J. M., Ottenhoff, R., Powlson, A. S., Grefhorst, A., Van Eijk, M., Dubbelhuis, P. F., … Overkleeft, H. S. (2007). Pharmacological inhibition of glucosylceramide synthase enhances insulin sensitivity. Diabetes, 56(5). https://doi.org/10.2337/db06-1619

27.Baccam, G.C., Xie, J., Jin, X. et al. Glucosylceramide synthase inhibition protects against cardiac hypertrophy in chronic kidney disease. Sci Rep 12, 9340 (2022). https://doi.org/10.1038/s41598-022-13390-z

28. Bikman, B. T., & Summers, S. A. (2011). Ceramides as modulators of cellular and whole-body metabolism. Journal of Clinical Investigation, Vol. 121. https://doi.org/10.1172/JCI57144

29. Turpin-Nolan, S. M., & Brüning, J. C. (2020). The role of ceramides in metabolic disorders: when size and localization matters. Nature Reviews Endocrinology, Vol. 16. https://doi.org/10.1038/s41574-020-0320-5

30. Roger Sandhoff, Heike Schulze, Konrad Sandhoff. (2018).Chapter One - Ganglioside Metabolism in Health and Disease,Editor(s): Ronald L. Schnaar, Pablo H.H. Lopez. Progress in Molecular Biology and Translational Science,Academic Press,Volume 156, Pages 1-62, ISSN 1877-1173,ISBN 9780128123416, https://doi.org/10.1016/bs.pmbts.2018.01.002.

31. Dhar, M. S., Sommardahl, C. S., Kirkland, T., Nelson, S., Donnell, R., Johnson, D. K., & Castellani, L. W. (2004). Mice Heterozygous for Atp10c, A Putative Amphipath, Represent A Novel Model of Obesity and Type 2 Diabetes. Journal of Nutrition, 134(4). https://doi.org/10.1093/jn/134.4.799

32. Dhar, M. S., Yuan, J. S., Elliott, S. B., & Sommardahl, C. (2006). A type IV P-type ATPase affects insulin-mediated glucose uptake in adipose tissue and skeletal muscle in mice. Journal of Nutritional Biochemistry. https://doi.org/10.1016/j.jnutbio.2006.01.002

33. Kayashima, T., Ohta, T., Niikawa, N., Kishino, T., & Oshimura, M. (2003). On the conflicting reports of imprinting status of mouse ATP10a in the adult brain: Strain-background-dependent imprinting? (multiple letters). *Journal of Human Genetics*, Vol. 48. https://doi.org/10.1007/s10038-003-0061-z

34. Hogart, A., Patzel, K. A., & LaSalle, J. M. (2008). Gender influences monoallelic expression of ATP10A in human brain. *Human Genetics*, *124*(3). https://doi.org/10.1007/s00439-008-0546-0

35. DuBose, A. J., Johnstone, K. A., Smith, E. Y., Hallett, R. A. E., & Resnick, J. L. (2010). Atp10a, a gene adjacent to the PWS/AS gene cluster, is not imprinted in mouse and is insensitive to the PWS-IC. *Neurogenetics*. https://doi.org/10.1007/s10048-009-0226-9

36. Hurst, S. E., Minkin, S. C., Biggerstaff, J., & Dhar, M. S. (2012). Transient silencing of a type IV P-type ATPase, Atp10c, results in decreased glucose uptake in C2C12 myotubes. Journal of Nutrition and Metabolism, 2012. https://doi.org/10.1155/2012/152902

37. Bhattacharyya, S., Luan, J., Challis, B., Keogh, J., Montague, C., Brennand, J., … O'Rahilly, S. (2006). Sequence variants in the melatonin-related receptor gene (GPR50) associate with circulating triglyceride and HDL levels. *Journal of Lipid Research*, *47*(4). https://doi.org/10.1194/jlr.M500338-JLR200

38. Ivanova, E. A., Bechtold, D. A., Dupré, S. M., Brennand, J., Barrett, P., Luckman, S. M., & Loudon, A. S. I. (2008). Altered metabolism in the melatonin-related receptor (GPR50) knockout mouse. *American Journal of Physiology - Endocrinology and Metabolism*, *294*(1). https://doi.org/10.1152/ajpendo.00199.2007

39. Yao, Z., Meng, J., Long, J., Li, L., Qiu, W., Li, C., … Ren, P. G. (2023). Orphan receptor GPR50 attenuates inflammation and insulin signaling in 3T3-L1 preadipocytes. *FEBS Open Bio*, *13*(1). https://doi.org/10.1002/2211-5463.13516

40. Wang, R., Zhang, P., Wang, J., Ma, L., E, W., Suo, S., … Han, X. (2023). Construction of a cross-species cell landscape at single-cell level. *Nucleic Acids Research*, *51*(2). https://doi.org/10.1093/nar/gkac633

41. Guilliams, M., Bonnardel, J., Haest, B., Vanderborght, B., Wagner, C., Remmerie, A., … Scott, C. L. (2022). Spatial proteogenomics reveals distinct and evolutionarily conserved hepatic macrophage niches. *Cell*, *185*(2). https://doi.org/10.1016/j.cell.2021.12.018

42. Stern, M. P. (1995). Diabetes and cardiovascular disease: The "common soil" hypothesis. *Diabetes*, Vol. 44. https://doi.org/10.2337/diab.44.4.369

43. Ginsberg, H. N. (2000). Insulin resistance and cardiovascular disease. *Journal of Clinical Investigation*, Vol. 106. https://doi.org/10.1172/JCI10762

44. Nozaki, Y., Fujita, K., Wada, K., Yoneda, M., Shinohara, Y., Imajo, K., … Nakajima, A. (2015). Deficiency of eNOS exacerbates early-stage NAFLD pathogenesis by changing the fat distribution. *BMC Gastroenterology*, *15*(1). https://doi.org/10.1186/s12876-015-0409-9

45. Huang, P. L., Huang, Z., Mashimo, H., Bloch, K. D., Moskowitz, M. A., Bevan, J. A., & Fishman, M. C. (1995). Hypertension in mice lacking the gene for endothelial nitric oxide synthase. *Nature*, *377*(6546). https://doi.org/10.1038/377239a0

46. Duplain, H., Burcelin, Ŕ., Sartori, C., Cook, S., Egli, M., Lepori, M., … Scherrer, U. (2001). Insulin resistance, hyperlipidemia, and hypertension in mice lacking endothelial nitric oxide synthase. *Circulation*, *104*(3). https://doi.org/10.1161/01.CIR.104.3.342

47. Pradines-Figueres, A., Vannier, C., & Ailhaud, G. (1988). Short-term stimulation by insulin of lipoprotein lipase secretion in adipose cells. *Biochemical and Biophysical Research Communications*, *154*(3). https://doi.org/10.1016/0006-291X(88)90236-7

48. Spooner, P. M., Chernick, S. S., Garrison, M. M., & Scow, R. O. (1979). Insulin regulation of lipoprotein lipase activity and release in 3T3-L1 adipocytes. Separation and dependence of hormonal effects on hexose metabolism and synthesis of RNA and protein. *Journal of Biological Chemistry*, *254*(20). https://doi.org/10.1016/s0021-9258(19)86667-x

49. Semenkovich, C. F., Wims, M., Noe, L., Etienne, J., & Chan, L. (1989). Insulin regulation of lipoprotein lipase activity in 3T3-L1 adipocytes is mediated at posttranscriptional and posttranslational levels. *Journal of Biological Chemistry*, *264*(15). https://doi.org/10.1016/s0021-9258(18)81898-1

50. Sadur, C. N., & Eckel, R. H. (1982). Insulin stimulation of adipose tissue lipoprotein lipase. Use of the euglycemic clamp technique. *Journal of Clinical Investigation*, *69*(5). https://doi.org/10.1172/JCI110547

51. Bijvoet, S., Gagné, S. E., Moorjani, S., Gagné, C., Henderson, H. E., Fruchart, J. C., … Hayden, M. R. (1996). Alterations in plasma lipoproteins and apolipoproteins before the age of

40 in heterozygotes for lipoprotein lipase deficiency. *Journal of Lipid Research*, Vol. 37. https://doi.org/10.1016/s0022-2275(20)37605-7

52. BRUNZELL, J. (1913). Familial Lipoprotein Lipase Deficiency and Other Causes of the Chylomicronemia Syndrome. *Scn'ver, C, Baudet. A., Sly, W., and Valle, D., eds. The Metabolite and Molecular Basis of Inherited Disease, 7th ed.(McGraw-I-Iill, New York) pp*, *1932*.

53. Young, M. E., Radda, G. K., & Leighton, B. (1997). Nitric oxide stimulates glucose transport and metabolism in rat skeletal muscle in vitro. *Biochemical Journal*, *322*(1). https://doi.org/10.1042/bj3220223

54. Etgen, G. J., Fryburg, D. A., & Gibbs, E. M. (1997). Nitric oxide stimulates skeletal muscle glucose transport through a calcium/contraction- and phosphatidylinositol-3-kinase-independent pathway. *Diabetes*, *46*(11). https://doi.org/10.2337/diab.46.11.1915

55. Konishi, M., Sakaguchi, M., Lockhart, S. M., Cai, W., Li, M. E., Homan, E. P., … Kahn, C. R. (2017). Endothelial insulin receptors differentially control insulin signaling kinetics in peripheral tissues and brain of mice. *Proceedings of the National Academy of Sciences of the United States of America*, *114*(40). https://doi.org/10.1073/pnas.1710625114

56. Kim, F., Pham, M., Maloney, E., Rizzo, N. O., Morton, G. J., Wisse, B. E., … Schwartz, M. W. (2008). Vascular inflammation, insulin resistance, and reduced nitric oxide production precede the onset of peripheral insulin resistance. *Arteriosclerosis, Thrombosis, and Vascular Biology*, *28*(11). https://doi.org/10.1161/ATVBAHA.108.169722

57.Zhao, L., Fu, Z., Wu, J., Aylor, K. W., Barrett, E. J., Cao, W., & Liu, Z. (2015). Inflammation-induced microvascular insulin resistance is an early event in diet-induced obesity. *Clinical Science*, *129*(12). https://doi.org/10.1042/CS20150143

58. Tsuchiya, K., & Accili, D. (2013). Liver sinusoidal endothelial cells link hyperinsulinemia to hepatic insulin resistance. *Diabetes*, *62*(5). https://doi.org/10.2337/db12-1296

59. Kadry, H., Noorani, B., & Cucullo, L. (2020). A blood–brain barrier overview on structure, function, impairment, and biomarkers of integrity. *Fluids and Barriers of the CNS*, Vol. 17. https://doi.org/10.1186/s12987-020-00230-3

60. Barrett, E. J., Wang, H., Upchurch, C. T., & Liu, Z. (2011). Insulin regulates its own delivery to skeletal muscle by feed-forward actions on the vasculature. *American Journal of Physiology - Endocrinology and Metabolism*, Vol. 301. https://doi.org/10.1152/ajpendo.00186.2011

61. Barter, P. J., & Nestel, P. J. (1973). Precursors of plasma triglyceride fatty acids in obesity. *Metabolism*, *22*(6). https://doi.org/10.1016/0026-0495(73)90048-6

62. Kissebah, A. H., Alfarsi, S., Adams, P. W., & Wynn, V. (1976). Role of insulin resistance in adipose tissue and liver in the pathogenesis of endogenous hypertriglyceridaemia in man. *Diabetologia*, *12*(6). https://doi.org/10.1007/BF01220632

63. Lewis GF. Lipid metabolism. Curr Opin Lipidol. 1999 Oct;10(5):475-7. PMID: 10554711.

64.La Rose, A. M., Bazioti, V., & Westerterp, M. (2018). Adipocyte Membrane Cholesterol Regulates Obesity. *Arteriosclerosis, Thrombosis, and Vascular Biology*, Vol. 38. https://doi.org/10.1161/ATVBAHA.118.310768

65. Sato, H., Taketomi, Y., Ushida, A., Isogai, Y., Kojima, T., Hirabayashi, T., … Murakami, M. (2014). The adipocyte-inducible secreted phospholipases PLA2G5 and PLA2G2E play distinct roles in obesity. *Cell Metabolism*, *20*(1). https://doi.org/10.1016/j.cmet.2014.05.002

66. Garcia, D., & Shaw, R. J. (2017). AMPK: Mechanisms of Cellular Energy Sensing and Restoration of Metabolic Balance. *Molecular Cell*, Vol. 66. https://doi.org/10.1016/j.molcel.2017.05.032

67.Asztalos, B. F., Tani, M., & Schaefer, E. J. (2011). Metabolic and functional relevance of HDL subspecies. *Current Opinion in Lipidology*, *22*(3). https://doi.org/10.1097/MOL.0b013e3283468061

68. Hanafi, N. I., Mohamed, A. S., Kadir, S. H. S. A., & Othman, M. H. D. (2018). Overview of bile acids signaling and perspective on the signal of ursodeoxycholic acid, the most hydrophilic bile acid, in the heart. *Biomolecules*, Vol. 8. https://doi.org/10.3390/biom8040159

69. Crimmins, E. M., Shim, H., Zhang, Y. S., & Kim, J. K. (2019). Differences between men and women in mortality and the health dimensions of the morbidity process. *Clinical Chemistry*, Vol. 65. https://doi.org/10.1373/clinchem.2018.288332

70. Cid, M. C., Schnaper, H. W., & Kleinman, H. K. (2002). Estrogens and the vascular endothelium. *Annals of the New York Academy of Sciences*, *966*. https://doi.org/10.1111/j.1749-6632.2002.tb04211.x

71. Mohan, S., Reddick, R. L., Musi, N., Horn, D. A., Yan, B., Prihoda, T. J., … Abboud-Werner, S. L. (2008). Diabetic eNOS knockout mice develop distinct macro- and microvascular complications. *Laboratory Investigation*, *88*(5). https://doi.org/10.1038/labinvest.2008.23

72. Mitchell, J. A., & Kirkby, N. S. (2019). Eicosanoids, prostacyclin and cyclooxygenase in the cardiovascular system. *British Journal of Pharmacology*, Vol. 176. https://doi.org/10.1111/bph.14167

73. Yamaguchi A, Botta E and Holinstat M (2022) Eicosanoids in inflammation in the blood and the vessel. Front. Pharmacol. 13:997403. doi: 10.3389/fphar.2022.997403

74. Chalfant, C. E., & Spiegel, S. (2005). Sphingosine 1-phosphate and ceramide 1-phosphate: Expanding roles in cell signaling. *Journal of Cell Science*, *118*(20). https://doi.org/10.1242/jcs.02637

75. Han, M. S., Lim, Y. M., Quan, W., Kim, J. R., Chung, K. W., Kang, M., … Lee, M. S. (2011). Lysophosphatidylcholine as an effector of fatty acid-induced insulin resistance. *Journal of Lipid Research*, *52*(6). https://doi.org/10.1194/jlr.M014787

76. Butler, M. G. (2020). Imprinting disorders in humans: a review. *Current Opinion in Pediatrics*, Vol. 32. https://doi.org/10.1097/MOP.0000000000000965

77. May, J. C., Goodwin, C. R., Lareau, N. M., Leaptrot, K. L., Morris, C. B., Kurulugama, R. T., … McLean, J. A. (2014). Conformational ordering of biomolecules in the gas phase: Nitrogen collision cross sections measured on a prototype high resolution drift tube ion mobility-mass spectrometer. *Analytical Chemistry*, *86*(4). https://doi.org/10.1021/ac4038448

78. Rose, B. S., May, J. C., Picache, J. A., Codreanu, S. G., Sherrod, S. D., & Mclean, J. A. (2022). Improving confidence in lipidomic annotations by incorporating empirical ion mobility regression analysis and chemical class prediction. *Bioinformatics*, *38*(10). https://doi.org/10.1093/bioinformatics/btac197

79. Yazlovitskaya, E. M., Plosa, E., Bock, F., Viquez, O. M., Mernaugh, G., Gewin, L. S., … Zent, R. (2021). The laminin-binding integrins regulate nuclear factor κB-dependent epithelial cell polarity and inflammation. *Journal of Cell Science*, *134*(24). https://doi.org/10.1242/jcs.259161

80. FOLCH, J., LEES, M., & SLOANE STANLEY, G. H. (1957). A simple method for the isolation and purification of total lipides from animal tissues. *The Journal of Biological Chemistry*, *226*(1). https://doi.org/10.1016/s0021-9258(18)64849-5

81. Morrison, W. R., & Smith, L. M. (1964). Preparation of fatty acid methyl esters and dimethylacetals from lipids with boron fluoride–methanol. *Journal of Lipid Research*, *5*(4). https://doi.org/10.1016/s0022-2275(20)40190-7

82. Sud, M., Fahy, E., Cotter, D., Azam, K., Vadivelu, I., Burant, C., … Subramaniam, S. (2016). Metabolomics Workbench: An international repository for metabolomics data and metadata, metabolite standards, protocols, tutorials and training, and analysis tools. *Nucleic Acids Research*, *44*(D1). https://doi.org/10.1093/nar/gkv1042

83. Zhang, B. B., Zhou, G., & Li, C. (2009). AMPK: an emerging drug target for diabetes and the metabolic syndrome. *Cell metabolism*, *9*(5), 407–416. https://doi.org/10.1016/j.cmet.2009.03.012

**Figure Legends**

Figure 1. ***Atp10A* deletion does not cause diet-induced obesity or changes to glucose homeostasis after 12 weeks of HFD.** (A) Graphic illustrating how CRISPR/cas9 was used to delete exon 2 in the mouse *Atp10A* to create the *Atp10A*$^{-/-}$ (KO) mouse line. (B) Weight gain of male and female *Atp10A*$^{+/+}$ (*10A*$^{+/+}$) and *Atp10A*$^{-/-}$ (*10A*$^{-/-}$) mice over the course of 12 weeks on a HFD (60 kcal% fat, Ad lib feeding), P value by 2-way ANOVA with Sidak's multiple comparison. (**Male:** *10A*$^{+/+}$ n=17, *10A*$^{-/-}$ n=15; **Female:** *10A*$^{+/+}$ n=34, *10A*$^{-/-}$ n=31) (C) Lean and (D) fat body mass were normalized to the combined sum of lean and fat mass to calculate % Lean and % Fat mass, P value by unpaired t-test (**Male**: *10A*$^{+/+}$ n=11,*10A*$^{-/-}$ n=13; **Female**:*10A*$^{+/+}$ n=13,*10A*$^{-/-}$ n=14). (E) Fasting blood glucose was measured from tail blood after a 5 hour fast, via a glucometer, P value by unpaired t-test **(Male:** *10A*$^{+/+}$ n=10, *10A*$^{-/-}$ n=11; **Female**: *10A*$^{+/+}$ n=19, *10A*$^{-/-}$ n=14). (F) Fasting plasma insulin was measured after a 5 hour fast, P value by unpaired t-test (**Male:** *10A*$^{+/+}$ n=8, *10A*$^{-/-}$ n=10; **Female:** *10A*$^{+/+}$ n=13,*10A*$^{-/-}$ n=9). (G) Male and (H) female mice were gavaged with 20% dextrose (time 0 on the graph) after a 5-hour fast then an oral glucose tolerance test (OGTT) was performed. The inset shows the area under the curve (AUC) normalized to fasting blood glucose (points before time 0 on the graph). OGTT, P value by 2-way ANOVA with Sidak's multiple comparison, AUC, P value by unpaired t-test (**Male:** *10A*$^{+/+}$ n=6,*10A*$^{-/-}$ n=6; **Female**: *10A*$^{+/+}$ n=12, *10A*$^{-/-}$ n=6).

---

Figure 2. ***Atp10A* deletion causes diet-induced dyslipidemia in female mice.** (A-F) Free fatty acids (FFA), cholesterol (chol), and triglycerides (TG) were measured in plasma from

males (A-C) or females (D-F) after a 5 hour fast or after a 5 hour fast followed by an OGTT. P value by unpaired t-test. (A, *10A*$^{+/+}$ n=7, *10A*$^{-/-}$ n=6; B, *10A*$^{+/+}$ n=8, *10A*$^{-/-}$ n=6; C, *10A*$^{+/+}$ n=9, *10A*$^{-/-}$ n=7; D, *10A*$^{+/+}$ n=12, *10A*$^{-/-}$ n=9,*P=0.0320; E, *10A*$^{+/+}$ n=12, *10A*$^{-/-}$ n=9, **P=0.0030; F, *10A*$^{+/+}$ n=12, *10A*$^{-/-}$ n=9, *P=0.0165.) (G-I) Lipoproteins in pooled plasma from females, collected after a 5-hour fast or 5-hour fast and OGTT, were separated via FPLC (G). Plasma TG (purple) and cholesterol (blue) content were measured from the separated lipoproteins, LDL=low density lipoprotein. AUC of TG fractions 10-18 of VLDL (H) and cholesterol fractions 30-50 of HDL (I) are from panel G. P value by unpaired t-test (**TG:***10A*$^{+/+}$ n=6, *10A*$^{-/-}$ n=7, **Chol:***10A*$^{+/+}$ n=6, *10A*$^{-/-}$ n=6).

---

Figure 3. ***Atp10A* deletion leads to substantial perturbations in the plasma lipidome and visceral fat transcriptome in female mice on a HFD**. (A) Lipid metabolites from fasting plasma were measured by HPLC-IM-MS/MS and the data was processed via Progenesis QI. The table indicates the number of total and significantly changed lipid metabolites (compounds) observed from each ionization mode (Negative and Positive); the volcano plot illustrates the fold changes (FC) of compounds between *10A*$^{-/-}$ vs. *10A*$^{+/+}$ mice, the grey shading indicates changes that did not meet the significance criteria. P-values by ANOVA. (*10A*$^{+/+}$ n=5 samples (8 mice), *10A*$^{-/-}$ n=5 samples (8 mice). (B) The log2(FoldChange) of lipid metabolites compared between *10A*$^{-/-}$ vs. *10A*$^{+/+}$ mice are grouped by indicated categories (green and blue indicate the % of lipid species with positive and negative fold change, respectively, between *10A*$^{-/-}$ vs. *10A*$^{+/+}$ mice; P values $\leq$ 0.1 by ANOVA). (C) Sequencing of visceral fat mRNA was performed using the Illumina NovaSeq 6000. The table provides the criteria used to calculate the number of differentially expressed genes (DEGs) and how many DEGs were measured; the volcano plot illustrates the DEGs (*10A*$^{+/+}$ n=3,*10A*$^{-/-}$ n=3). (D) Schematic illustrating the metabolic pathways linking ATP10A substrates to observed changes in the plasma lipidome and visceral fat

transcriptome. Lipid metabolites with significant changes due to *10A* deletion from panel B are in bold red, the hexosylceramide category includes both GalCer and GlcCer. The protein products from two mRNA transcripts that were significantly upregulated in the visceral fat from *10A*$^{-/-}$ mice (panel C), Pla2G5 and Lipf, are highlighted to show their role in lipid metabolism. Schematic created using Biorender.com. See Supplemental Table 2 for RNASeq KEGG pathway analysis. PC= phosphatidylcholine, AA=arachidonic acid, TG= triglyceride, FA=fatty acids, FFA=free fatty acids, DAG=diacylglycerol, MAG=monoacylglycerol, SM=sphingomyelin, S1P= sphingosine 1-phosphate, C1P= ceramide 1-phosphate, GalCer= galactosylceramide, GlcCer= glucosylceramide.

---

Figure 4. ***Atp10A* deletion perturbs liver insulin signaling in female mice fed a HFD.** (A, D) Representative blots for total and/or phosphorylated (A) DGAT1, DGAT2, AMPKα, ACC, and (D) IRβ, IRS-1, Akt, GSK-3β, and $cPLA_2$. (B) For DGAT1 and DGAT2 quantitation, total protein was normalized to β-actin levels. (C, E) The phosphoproteins were normalized to their respective total protein and β-actin levels. Mean measurements of 4-6 independent experiments are shown. P value by (B, C) unpaired t-test or (E) 2-way ANOVA with Sidak's multiple comparison test. (A-C, *10A*$^{+/+}$ n=7, *10A*$^{-/-}$ n=7, B: **P=0.0050; C: *P=0.0229, *P=0.0481; D, E, *10A*$^{+/+}$ n=8, *10A*$^{-/-}$ n=8, **P=0.0044, ***P=0.0007, **P=0.0038, ****P=<0.0001,). (F) Schematic adapted from (83) and created using Biorender.com. The illustration shows insulin binding to the insulin receptor and the resulting downstream signaling events that stimulate lysoPC production, AA metabolism, changes to glucose and lipid metabolism; including the promotion of lipogenesis. MAPK= mitogen-activated protein kinase, $cPLA_2$= cytosolic phospholipase 2, IRS-1= insulin receptor substrate 1, PI3K= phosphoinositide 3-kinase, PIP2=phosphatidylinositol 4,5-bisphosphate, PIP3= phosphatidylinositol 3,4,5-triphosphate, PDK1= pyruvate dehydrogenase kinase 1, GSK-3β= glycogen synthase kinase-3 beta, LKB1= liver kinase B1,

AMPKα= AMP-activated protein kinase alpha, MCD= malonyl-CoA decarboxylase, ACC1=acetyl-CoA carboxylase, SCD1= stearoyl-CoA desaturase 1, MGAT=monoglycerol acyltransferase, DGAT= diglyceride acyltransferase.

---

Figure 5. **ATP10A is expressed in endothelial cells.** (A) Total tissue lysates from the *10A*$^{+/+}$ and *10A*$^{-/-}$ mice (vas deferens,testes, heart - males; brain, liver, visceral fat - females) were subjected to Western immunoblot analysis for expression of ATP10A (100 µg total protein). ATP10A migrates as a high-molecular-weight smear in the tissue samples. β-actin and GAPDH served as loading controls. The asterisk indicates a nonspecific band that appears in some samples. (B) Representative immunofluorescent images of vas deferens showing expression of ATP10A and DAPI. Scale bar= 40 µm. The white asterisk indicates background staining (*10A*$^{+/+}$ n=1, *10A*$^{-/-}$ n=1). (C) Representative immunofluorescent and colorimetric images of livers and visceral fat from females showing expression of ATP10A (fluorescence), CD31, and hematoxylin (colorimetric). Scale bar: fluorescent images=20 µm; colorimetric images= 40 µm. The white asterisk indicates background staining, the white arrows indicate locations that are positive for ATP10A expression (fluorescent) and CD31 expression (colorimetric) in sequential sections, the yellow arrows indicate auto fluorescent red blood cells (Liver: *10A*$^{+/+}$ n=3, *10A*$^{-/-}$ n=1; visceral fat: *10A*$^{+/+}$ n=3, *10A*$^{-/-}$ n=2). (D) Total lysates from routinely grown HUVEC and SVEC4-10 were subjected to Western immunoblot analysis for expression of ATP10A (50 µg total protein). β-actin served as loading control. (E) Representative immunofluorescent images of routinely grown HUVEC and SVEC4-10 showing expression of ATP10A and DAPI. Scale bar=10 µm.

---

Figure 6. **ATP10A expression regulates insulin signaling pathways in cultured endothelial cells and mouse aorta.** (A) Representative blots and (B) quantitative analysis from immunoblots of phosphorylated and total IRβ, IRS-1, Akt, eNOS, GSK-3β, and $cPLA_2$ from HUVEC transfected with non-silencing siRNA or ATP10A siRNA and then treated with 100 nM insulin for 0-60 mins. (C,D) Quantitative analysis of immunoblots at time 0 from (C) HUVEC or (D) SVEC4-10. (E) Representative blots and (F) quantitative analysis from immunoblots of phosphorylated and total eNOS from total aorta lysates from female mice ($10A^{+/+}$ n=5, $10A^{-/-}$ n=4, *P=0.0290). Mean measurements of 3-6 independent experiments are shown. (B-D) *p≤0.05; **p≤0.005; ***p≤0.0005 between cells transfected with non-silencing or ATP10A siRNA by 2-way ANOVA with Sidak's multiple comparison test, (F) P value by unpaired t-test.

---

Figure 7. **Model of ATP10A's role in metabolism.** (A) Schematic illustrating ATP10A maintaining insulin sensitivity in ECs. Left panel: WT ATP10A in ECs blocks IR/IGF1R signaling, via an unknown mechanism, during basal levels of insulin and downstream of this; the tissues associated with the ECs (hepatocytes and adipocytes) also maintain their sensitivity to insulin. Right panel: When ATP10A is knocked out/down; ECs lose their sensitivity to insulin stimulus due to IR/IGF1R inappropriately responding to basal levels of insulin, downstream of this the tissues associated with the ECs could also lose their sensitivity to insulin stimulus (become insulin resistant). (B) Schematic illustrating ATP10A's proposed function specifically at the plasma membrane (what is being magnified by magnifying glass in (A)). ATP10A translocates PC and GlcCer from the outer leaflet to the inner leaflet, this could potentially affect how lipoproteins interact with the plasma membrane, the lipid platforms where proteins reside (insulin receptor), and the abundance of bioactive lipid species in the cytosolic space (that could

also potentially affect IR/IGFR1 signaling). Schematics created using Biorender.com. LPL=lipoprotein lipase, NO=nitric oxide.

---

Supplemental Figure 1. ***Atp10A* KO female mice have smaller bodies on the 12th week of the HFD.** (A) Body length of mice was measured after $CO_2$ sacrifice. P value by unpaired t-test, **P=0.0094. (**Male:** *10A*$^{+/+}$ n=11, *10A*$^{-/-}$ n=5; **Female**: *10A*$^{+/+}$ n=17, *10A*$^{-/-}$ n=14). (B)The wet mass of tissue was measured after removal from female mice on the 12th week on the HFD. Tissue mass is normalized to body mass. P value by unpaired t-tests. (*10A*$^{+/+}$ n=3-5,*10A*$^{-/-}$ n=7). Insulin was measured from serum collected during the OGTT shown in Figure 1G,H at the (C) 30 minute time point (T30) and the (D) 60 minute time point (T60), P value by unpaired t-test. (**Male:** C: *10A*$^{+/+}$ n=4, *10A*$^{-/-}$ n=4, D: *10A*$^{+/+}$ n=6, *10A*$^{-/-}$ n=5; **Female**: *10A*$^{+/+}$ n=8, *10A*$^{-/-}$ n=6).

---

Supplemental Figure 2. ***Atp10A* deletion causes alterations to average daily food intake and energy balance during the light hours in female mice fed a HFD for 13 weeks.** The table indicates the parameters measured in the Sable System's Promethion Indirect Calorimetry System where the mice were single-housed. The values are an average measurement from 5 days in the system with ad libitum feeding. P value by unpaired t-test (*10A*$^{+/+}$ n=7, *10A*$^{-/-}$ n=13).

---

Supplemental Figure 3. ***Atp10A* deletion does not affect weight gain, body composition, or glucose homeostasis in female mice after 12 weeks on normal chow.** (A) Weight gain of *10A*$^{+/+}$ and *10A*$^{-/-}$ female mice over the course of 12 weeks on normal chow (4.5 kcal% fat, Ad lib feeding), P value by 2-way ANOVA with Sidak's multiple comparison. (*10A*$^{+/+}$ n=4,*10A*$^{-/-}$ n=7).

(B) Lean and (C) fat body mass was normalized to the combined sum of lean and fat mass to calculate % Lean and % Fat mass. P value by unpaired t-test (*10A*$^{+/+}$ n=4, *10A*$^{-/-}$ n=4). (D) Body length of mice was measured after $CO_2$ sacrifice. P value by unpaired t-test (*10A*$^{+/+}$ n=4,*10A*$^{-/-}$ n=4). (E) Fasting blood glucose was measured a 5 hour fast, via a glucometer. P value by unpaired t-test (*10A*$^{+/+}$ n=4,*10A*$^{-/-}$ n=4). (F) Fasting plasma insulin was measured after a 5 hour fast. P-value by unpaired t test (*10A*$^{+/+}$ n=4,*10A*$^{-/-}$ n=4).

---

Supplemental Figure 4. **Maternally inherited *Atp10A* deletion leads to smaller bodies and elevated fasting blood glucose in male mice on the 12th week on the HFD.** (A) Weight gain of heterozygous males and females inheriting the KO allele maternally (Maternal Inheritance (Inh.), *10A*$^{+/-}$ dam X *10A*$^{+/+}$ sire) or paternally (Paternal Inh, *10A*$^{+/+}$ dam x *10A*$^{+/-}$ sire) over the course of 12 weeks on a HFD (60 kcal% fat, Ad lib feeding). P value by 2-way ANOVA with Sidak's multiple comparison. (**Males**: Maternal Inh.*10A*$^{+/-}$ n=7, Paternal Inh.*10A*$^{+/-}$ n=10; **Females**: Maternal Inh.*10A*$^{+/-}$ n=10, Paternal Inh.*10A*$^{+/-}$ n=6). (B) Lean and (C) fat body mass were normalized to the combined sum of lean and fat mass to calculate % Lean and % Fat mass. P value by unpaired t-test (**Male**: Maternal Inh.*10A*$^{+/-}$ n=7, Paternal Inh.*10A*$^{+/-}$ n=10; **Female**: Maternal Inh.*10A*$^{+/-}$ n=10, Paternal Inh.*10A*$^{+/-}$ n=6). (D) Body length of male mice was measured after $CO_2$ sacrifice. P value by unpaired t-test, *P=0.0490. (Maternal Inh.*10A*$^{+/-}$ n=4, Paternal Inh.*10A*$^{+/-}$ n=9). (E) Fasting blood glucose was measured after a 5 hour fast, via a glucometer. P value by unpaired t-test, **P=0.0081. (**Male**: Maternal Inh.*10A*$^{+/-}$ n=7, Paternal Inh.*10A*$^{+/-}$ n=10; **Female**: Maternal Inh.*10A*$^{+/-}$ n=10, Paternal Inh.*10A*$^{+/-}$ n=6). (F) Fasting plasma insulin was measured after a 5 hour fast, P value by unpaired t-test. (**Male**: Maternal Inh.*10A*$^{+/-}$ n=6, Paternal Inh.*10A*$^{+/-}$ n=10; **Female**: Maternal Inh.*10A*$^{+/-}$ n=5, Paternal Inh.*10A*$^{+/-}$ n=2).

---

Supplemental Figure 5. ***Atp10A* deletion causes changes to liver lipid metabolism in female mice after 12 weeks on a HFD.** (A-G) FFAs, Total cholesterol, cholesterol esters, unesterifed cholesterol, TGs, PLs, and ceramides were measured from flash frozen livers via gas chromatography. Livers were collected after a 5 hour fast or after a 5 hour fast followed by an OGTT. P value by unpaired t-test (FFA: *10A*$^{+/+}$ n=15,*10A*$^{-/-}$ n=7, *P=0.0201; Total cholesterol: *10A*$^{+/+}$ n=16, *10A*$^{-/-}$ n=7; Cholesterol esters: *10A*$^{+/+}$ n=6,*10A*$^{-/-}$ n=6; Unesterified cholesterol: *10A*$^{+/+}$ n=6,*10A*$^{-/-}$ n=6; TG: *10A*$^{+/+}$ n=14, *10A*$^{-/-}$ n=7; PLs: *10A*$^{+/+}$ n=16, *10A*$^{-/-}$ n=7; Ceramides: *10A*$^{+/+}$ n=16, *10A*$^{-/-}$ n=7). The saturation of liver (H) TG, PL, and (I) CE species was determined by gas chromatography. The fold change of unsaturated vs saturated TG, PL, CE is shown. P value by 2-way ANOVA with Sidak's multiple comparison, **TG**: **P=0.0025, ***P=0.0001, *P=0.0443, **PL**: *P=0.0297, *P=0.0281 (*10A*$^{+/+}$ n=16, *10A*$^{-/-}$ n=7). **CE:** P value by unpaired t-test, *P=0.0223 (*10A*$^{+/+}$ n=6, *10A*$^{-/-}$ n=6). (J) Representative images of livers stained with H+E (5x) or Oil Red O (63x). The coalescence of the Oil Red O stain is indicated by yellow asterisks (artifact) and the arrows point to neutral lipids stained by Oil Red O. Scale bars = 10 μM. (K) Liver sections were scored using the Oil Red O Score described in the Materials and Methods. P value by nonparametric t-test (Mann-Whitney U), *P=0.0327 (*10A*$^{+/+}$ n=6, *10A*$^{-/-}$ n=10). (L) The diameters of Oil Red O positive lipid droplets (LD) in the liver sections with a score of 2 were measured using ImageJ. The red line in the graph represents the SEM. P value by unpaired t-test, ****P=<0.0001 (*10A*$^{+/+}$,120 LDs measured, n=2, *10A*$^{-/-}$, 203 LDs measured, n=3).

---

Supplemental Figure 6. **Validation of anti-ATP10A antibody: expression of ATP10A in HeLa cells with over-expressed HA-ATP10A and in mouse heart.** (A) Table indicating the sequences of the ATP10A peptides that were injected into rabbits to produce antibodies. (B) Representative images of total cell lysates from HeLa cells with over-expressed HA-ATP10A

(40 µg total protein) that were subjected to Western immunoblot analyses for expression of ATP10A using antibody produced against ATP10A peptides (left and central panels) and HA (right panel). (C) Representative immunofluorescent images of hearts from female mice showing expression of ATP10A (green) and DAPI (blue). Scale bar = 20 µm. The white asterisk indicates background staining, the white arrow indicates ATP10A positive staining, the yellow arrow indicates auto fluorescent red blood cells (*10A*$^{+/+}$ n=1, *10A*$^{-/-}$ n=1).

---

Supplemental Figure 7. **ATP10A expression level regulates basal activity of insulin signaling pathways in endothelial cells.** (A,D) Representative images and quantitative analysis of ATP10A from immunoblots of HUVEC (A) and SVEC4-10 (D) untreated (c), transfected with non-silencing siRNA or ATP10A siRNA constructs (#1, #2, #1&#2). (B, E) Representative immunofluorescent images showing expression of ATP10A and DAPI in HUVEC (B) and SVEC4-10 (E) transfected with non-silencing siRNA (n) or ATP10A siRNA constructs (ATP10A#1, ATP10A#2, ATP10A#1&#2). Scale bar=10 µm. (C, F) Representative images of basal phosphorylated and total IRβ, IRS-1, Akt, eNOS, GSK-3β, and $cPLA_2$ from immunoblots of HUVEC (C) and SVEC4-10 (F) transfected with non-silencing siRNA or ATP10A#1&#2 siRNA constructs. Note that the lane between the non-silencing and ATP10A#1&#2 treated lanes contains the molecular weight marker.

---

Supplemental Figure 8. **ATP10A expression regulates insulin signaling pathway in SVEC4-10 cells and mouse aorta.** (A) Representative images and (B) quantitative analysis from immunoblots of phosphorylated and total IRβ, IRS-1, Akt, eNOS, GSK-3β, and $cPLA_2$ from SVEC4-10 cells transfected with non-silencing siRNA or ATP10A siRNA constructs and then treated with insulin for 0-60 mins. Mean measurements of 3-6 independent experiments are shown. *p≤0.05; **p≤0.005; ***p≤0.0005; ***p≤0.0001 between cells transfected with non-

silencing or ATP10A siRNA by 2-way ANOVA with Sidak's multiple comparison test. (C) Representative blots and (D) quantitative analysis from immunoblots of phosphorylated and total eNOS from total aorta lysates from male mice (*10A*$^{+/+}$ n=2, *10A*$^{-/-}$ n=4, statistics were not done due to low n). Mean measurements of 3-6 independent experiments are shown.

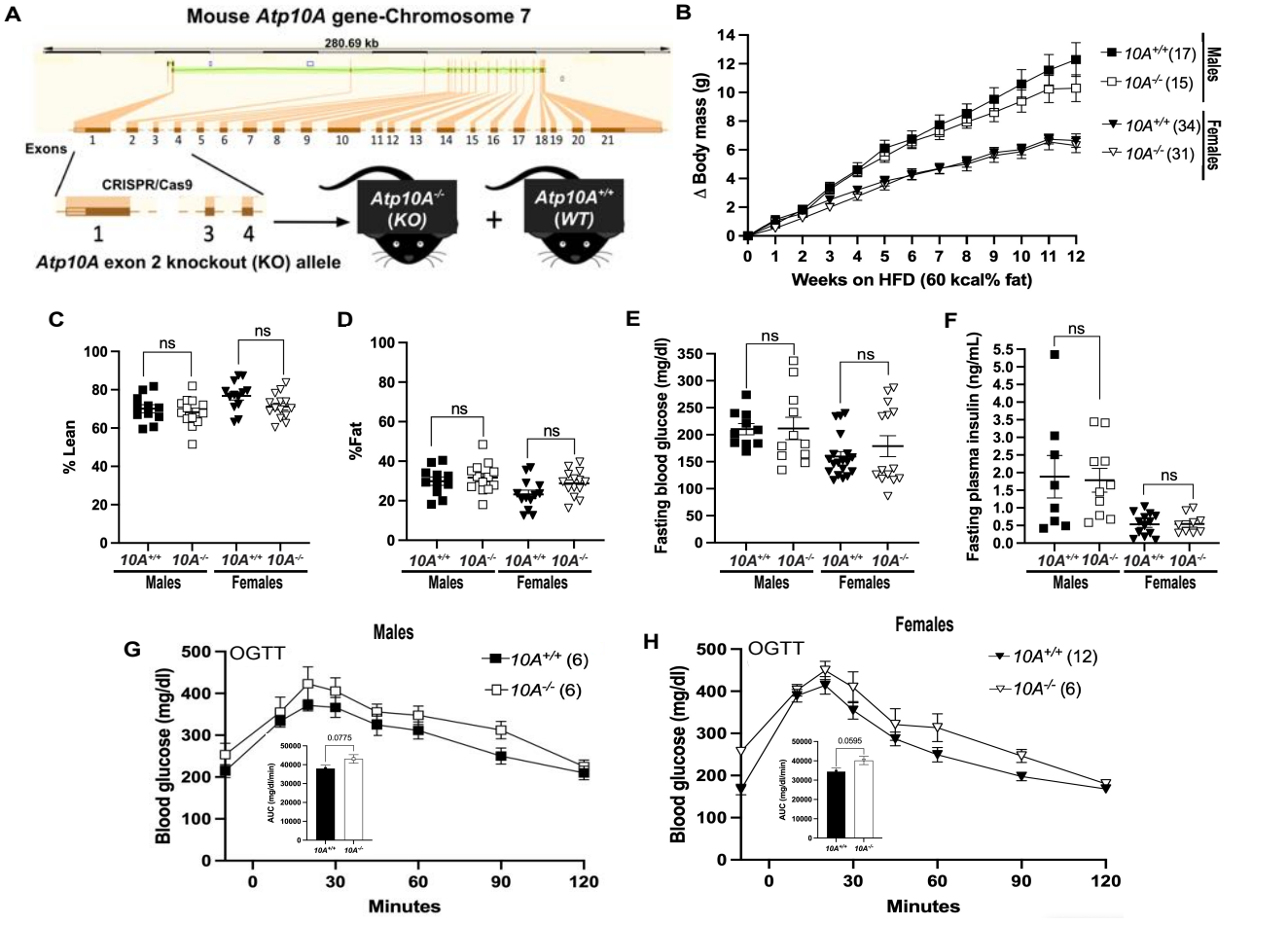


Figure 1. Atp10A deletion does not cause diet-induced obesity or changes to glucose homeostasis after 12 weeks of HFD. (A) Graphic illustrating how CRISPR/cas9 was used to delete exon 2 in the mouse Atp10A to create the Atp10A-/- (KO) mouse line. (B) Weight gain of male and female Atp10A+/+ (10A+/+) and Atp10A-/- (10A-/-) mice over the course of 12 weeks on a HFD (60 kcal% fat, Ad lib feeding), P value by 2-way ANOVA with Sidak's multiple comparison. (Male: 10A+/+ n=17, 10A-/- n=15; Female: 10A+/+ n=34, 10A-/- n=31) (C) Lean and (D) fat body mass were normalized to the combined sum of lean and fat mass to calculate % Lean and % Fat mass, P value by unpaired t-test (Male: 10A+/+ n=11,10A-/- n=13; Female:10A+/+ n=13,10A-/- n=14). (E) Fasting blood glucose was measured from tail blood after a 5 hour fast, via a glucometer, P value by unpaired t-test (Male: 10A+/+ n=10, 10A-/- n=11; Female: 10A+/+ n=19, 10A-/- n=14). (F) Fasting plasma insulin was measured after a 5 hour fast, P value by unpaired t-test (Male: 10A+/+ n=8, 10A-/- n=10; Female: 10A+/+ n=13,10A-/- n=9). (G) Male and (H) female mice were gavaged with 20% dextrose (time 0 on the graph) after a 5-hour fast then an oral glucose tolerance test (OGTT) was performed. The inset shows the area under the curve (AUC) normalized to fasting blood glucose (points before time 0 on the graph). OGTT, P value by 2-way ANOVA with Sidak's multiple comparison, AUC, P value by unpaired t-test (Male: 10A+/+ n=6,10A-/- n=6; Female: 10A+/+ n=12, 10A-/- n=6).

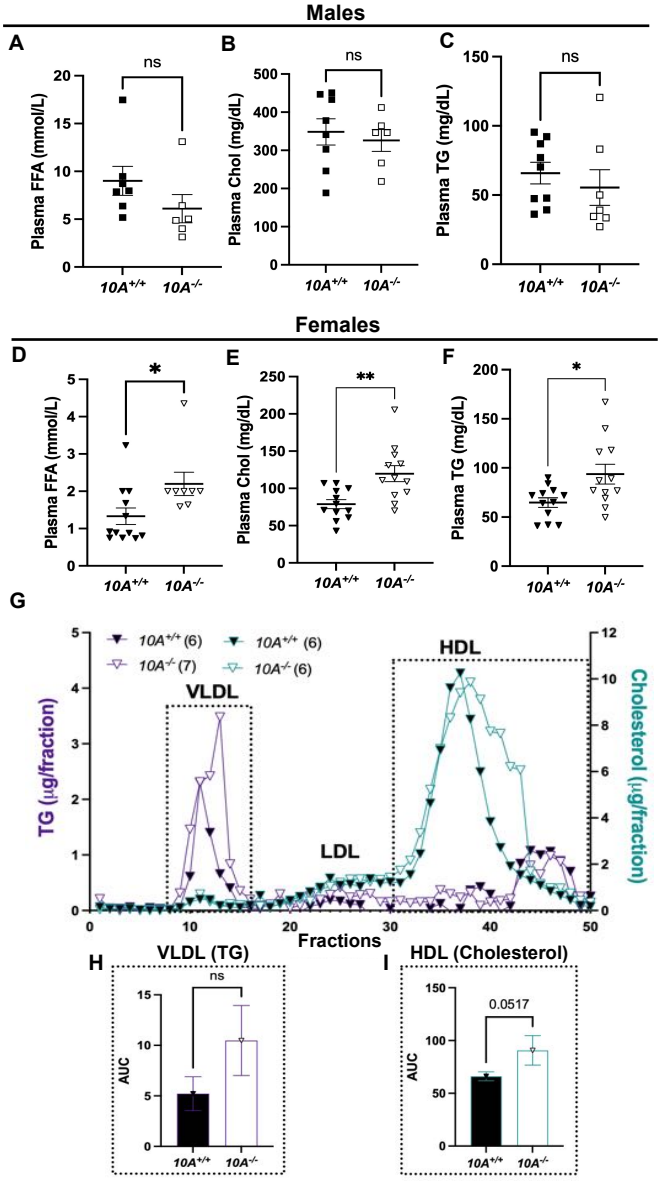


Figure 2. Atp10A deletion causes diet-induced dyslipidemia in female mice. (A-F) Free fatty acids (FFA), cholesterol (chol), and triglycerides (TG) were measured in plasma from males (A-C) or females (D-F) after a 5 hour fast or after a 5 hour fast followed by an OGTT. P value by unpaired t-test. (A, 10A+/+ n=7, 10A-/- n=6; B, 10A+/+ n=8, 10A-/- n=6; C, 10A+/+ n=9, 10A-/- n=7; D, 10A+/+ n=12, 10A-/- n=9,*P=0.0320; E, 10A+/+ n=12, 10A-/- n=9, **P=0.0030; F, 10A+/+ n=12, 10A-/- n=9, *P=0.0165.) (G-I) Lipoproteins in pooled plasma from females, collected after a 5-hour fast or 5-hour fast and OGTT, were separated via FPLC (G). Plasma TG (purple) and cholesterol (blue) content were measured from the separated lipoproteins, LDL=low density lipoprotein. AUC of TG fractions 10-18 of VLDL (H) and cholesterol fractions 30-50 of HDL (I) are from panel G. P value by unpaired t-test (TG:10A+/+ n=6, 10A-/- n=7, Chol:10A+/+ n=6, 10A-/- n=6).

**A**

| *10A-/- vs 10A+/+* | Negative | | Positive | |
|---|---|---|---|---|
| **Significance criteria: p ≤ 0.05 and FC ≥ \|2\|** | Total # of compounds | Total # of Significantly Altered Compounds | Total # of compounds | Total # of Significantly Altered Compounds |
| | 3318 | ***324*** | 3678 | ***267*** |

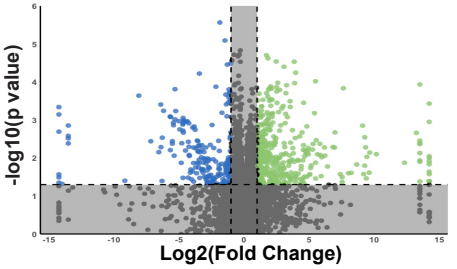


**B**

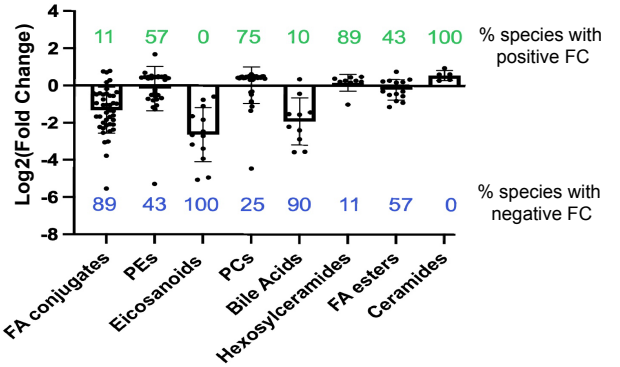


**C**

| *10A-/- vs 10A+/+* | Total DEGs | Down-regulated DEGs | Up-regulated DEGs |
|---|---|---|---|
| **DEG criteria: FDR ≤ 0.05 and FC ≥ \|2\|** | 166 | 29 | 137 |

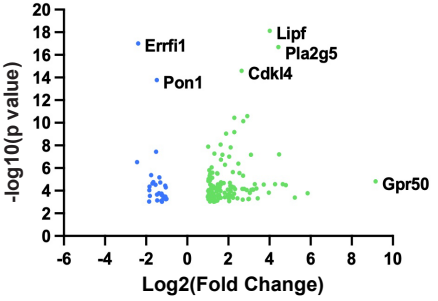


**D**

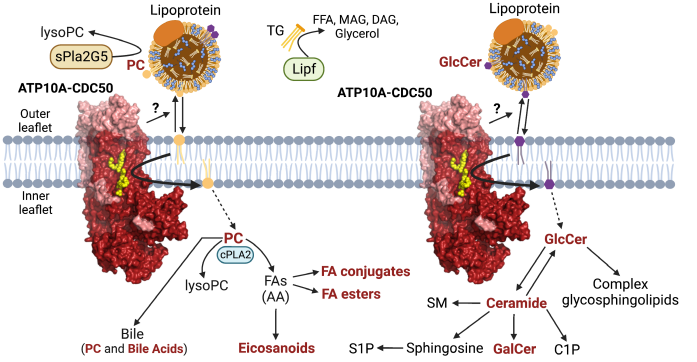


Figure 3. Atp10A deletion leads to substantial perturbations in the plasma lipidome and visceral fat transcriptome in female mice on a HFD. (A) Lipid metabolites from fasting plasma were measured by HPLC-IM-MS/MS and the data was processed via Progenesis QI. The table indicates the number of total and significantly changed lipid metabolites (compounds) observed from each ionization mode (Negative and Positive); the volcano plot illustrates the fold changes (FC) of compounds between 10A-/- vs. 10A+/+ mice, the grey shading indicates changes that did not meet the significance criteria. P-values by ANOVA. (10A+/+ n=5 samples (8 mice), 10A-/- n=5 samples (8 mice). (B) The log2(FoldChange) of lipid metabolites compared between 10A-/- vs. 10A+/+ mice are grouped by indicated categories (green and blue indicate the % of lipid species with positive and negative fold change, respectively, between 10A-/- vs. 10A+/+ mice; P values ≤ 0.1 by ANOVA). (C) Sequencing of visceral fat mRNA was performed using the Illumina NovaSeq 6000. The table provides the criteria used to calculate the number of differentially expressed genes (DEGs) and how many DEGs were measured; the volcano plot illustrates the DEGs (10A+/+ n=3,10A-/- n=3). (D) Schematic illustrating the metabolic pathways linking ATP10A substrates to observed changes in the plasma lipidome and visceral fat transcriptome. Lipid metabolites with significant changes due to 10A deletion from panel B are in bold red, the hexosylceramide category includes both GalCer and GlcCer. The protein products from two mRNA transcripts that were significantly upregulated in the visceral fat from 10A-/- mice (panel C), Pla2G5 and Lipf, are highlighted to show their role in lipid metabolism. Schematic created using Biorender.com. See Supplemental Table 2 for RNASeq KEGG pathway analysis. PC= phosphatidylcholine, AA=arachidonic acid, TG= triglyceride, FA=fatty acids, FFA=free fatty acids, DAG=diacylglycerol, MAG=monoacylglycerol, SM=sphingomyelin, S1P= sphingosine 1-phosphate, C1P= ceramide 1-phosphate, GalCer= galactosylceramide, GlcCer= glucosylceramide.

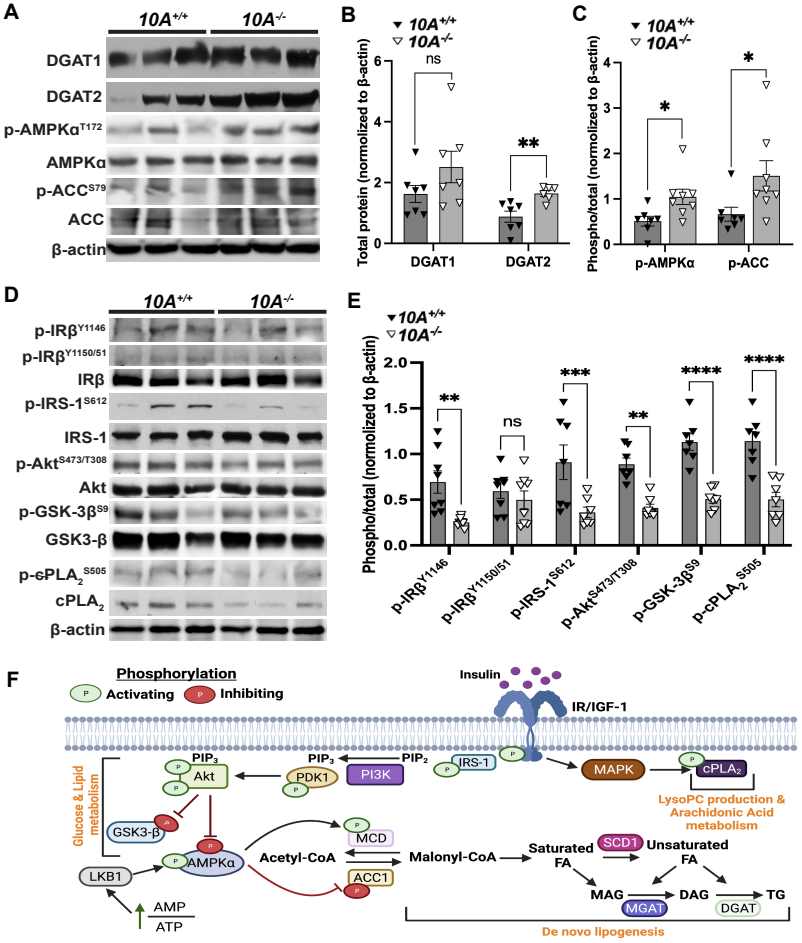


Figure 4. Atp10A deletion perturbs liver insulin signaling in female mice fed a HFD. (A, D) Representative blots for total and/or phosphorylated (A) DGAT1, DGAT2, AMPKα, ACC, and (D) IRβ, IRS-1, Akt, GSK-3β, and cPLA2. (B) For DGAT1 and DGAT2 quantitation, total protein was normalized to β-actin levels. (C, E) The phosphoproteins were normalized to their respective total protein and β-actin levels. Mean measurements of 4-6 independent experiments are shown. P value by (B, C) unpaired t-test or (E) 2-way ANOVA with Sidak's multiple comparison test. (A-C, 10A+/+ n=7, 10A-/- n=7, B: **P=0.0050; C: *P=0.0229, *P=0.0481; D, E, 10A+/+ n=8, 10A-/- n=8, **P=0.0044, ***P=0.0007, **P=0.0038, ****P=<0.0001,). (F) Schematic adapted from (83) and created using Biorender.com. The illustration shows insulin binding to the insulin receptor and the resulting downstream signaling events that stimulate lysoPC production, AA metabolism, changes to glucose and lipid metabolism; including the promotion of lipogenesis. MAPK= mitogen-activated protein kinase, cPLA2= cytosolic phospholipase 2, IRS-1= insulin receptor substrate 1, PI3K= phosphoinositide 3-kinase, PIP2=phosphatidylinositol 4,5-bisphosphate, PIP3= phosphatidylinositol 3,4,5-triphosphate, PDK1= pyruvate dehydrogenase kinase 1, GSK-3β= glycogen synthase kinase-3 beta, LKB1= liver kinase B1, AMPKα= AMP-activated protein kinase alpha, MCD= malonyl-CoA decarboxylase, ACC1=acetyl-CoA carboxylase, SCD1= stearoyl-CoA desaturase 1, MGAT=monoglycerol acyltransferase, DGAT= diglyceride acyltransferase.

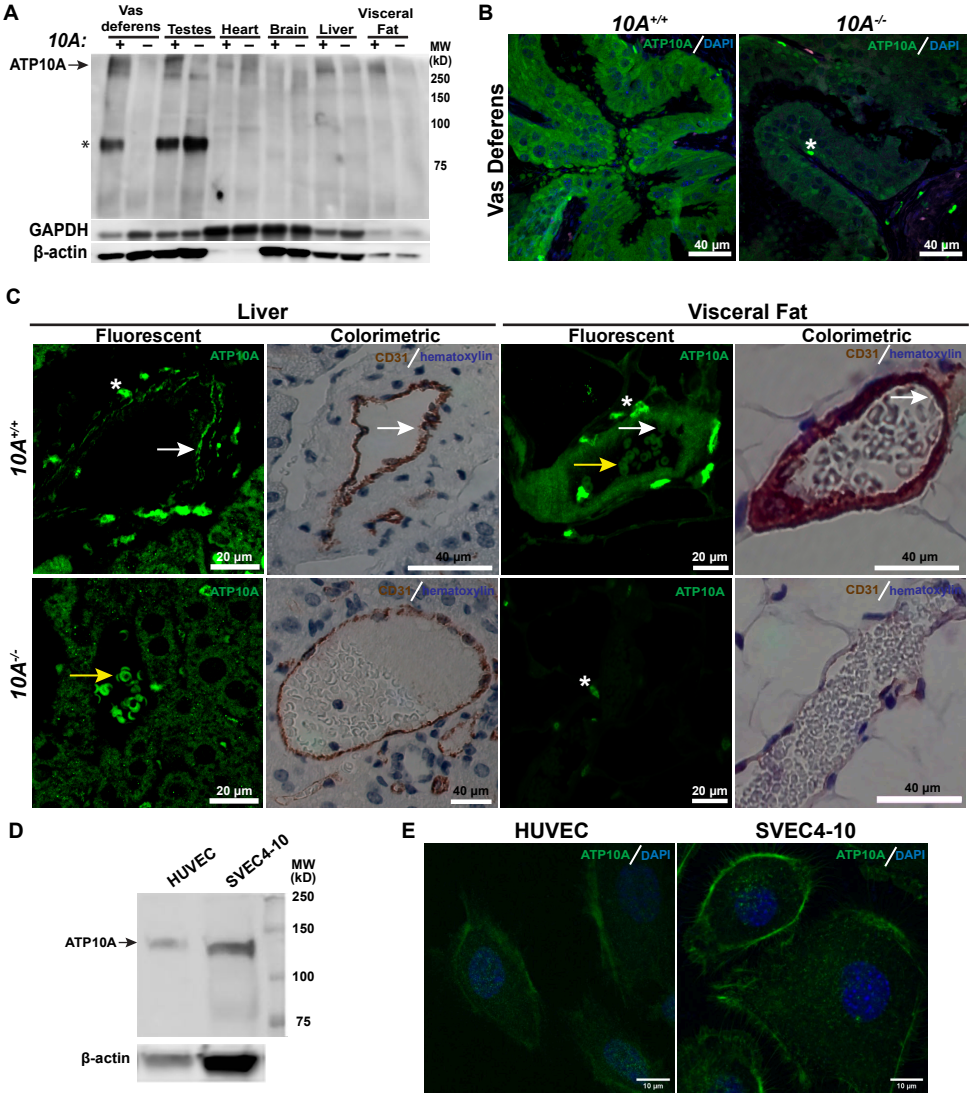


Figure 5. ATP10A is expressed in endothelial cells. (A) Total tissue lysates from the 10A+/+ and 10A-/- mice (vas deferens,testes, heart - males; brain, liver, visceral fat - females) were subjected to Western immunoblot analysis for expression of ATP10A (100 µg total protein). ATP10A migrates as a high-molecular-weight smear in the tissue samples. β-actin and GAPDH served as loading controls. The asterisk indicates a nonspecific band that appears in some samples. (B) Representative immunofluorescent images of vas deferens showing expression of ATP10A and DAPI. Scale bar= 40 µm. The white asterisk indicates background staining (10A+/+ n=1, 10A-/- n=1). (C) Representative immunofluorescent and colorimetric images of livers and visceral fat from females showing expression of ATP10A (fluorescence), CD31, and hematoxylin (colorimetric). Scale bar: fluorescent images=20 µm; colorimetric images= 40 µm. The white asterisk indicates background staining, the white arrows indicate locations that are positive for ATP10A expression (fluorescent) and CD31 expression (colorimetric) in sequential sections, the yellow arrows indicate auto fluorescent red blood cells (Liver: 10A+/+ n=3, 10A-/- n=1; visceral fat: 10A+/+ n=3, 10A-/- n=2). (D) Total lysates from routinely grown HUVEC and SVEC4-10 were subjected to Western immunoblot analysis for expression of ATP10A (50 µg total protein). β-actin served as loading control. (E) Representative immunofluorescent images of routinely grown HUVEC and SVEC4-10 showing expression of ATP10A and DAPI. Scale bar=10 µm.

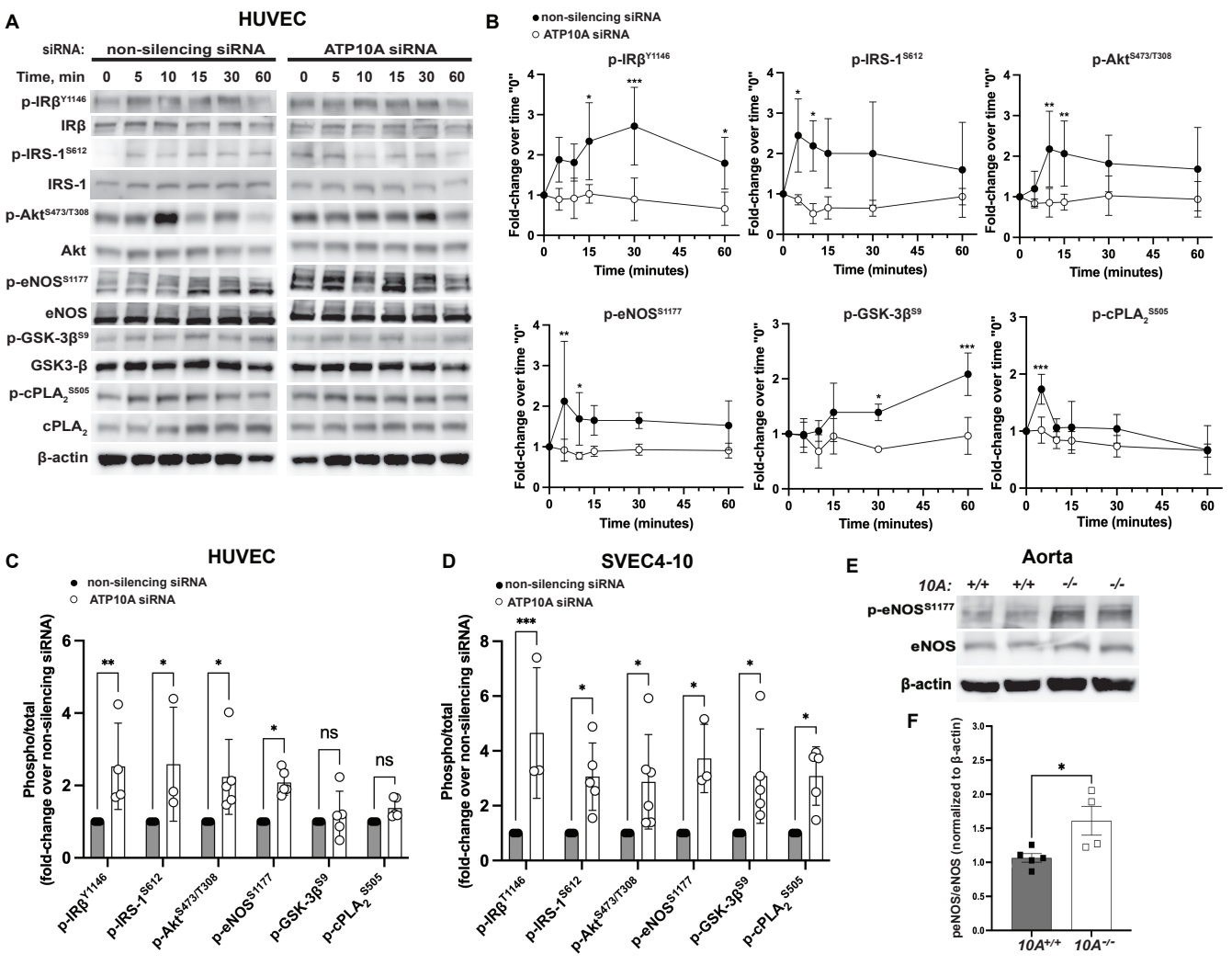


Figure 6. ATP10A expression regulates insulin signaling pathways in cultured endothelial cells and mouse aorta. (A) Representative blots and (B) quantitative analysis from immunoblots of phosphorylated and total IRβ, IRS-1, Akt, eNOS, GSK-3β, and cPLA2 from HUVEC transfected with non-silencing siRNA or ATP10A siRNA and then treated with 100 nM insulin for 0-60 mins. (C,D) Quantitative analysis of immunoblots at time 0 from (C) HUVEC or (D) SVEC4-10. (E) Representative blots and (F) quantitative analysis from immunoblots of phosphorylated and total eNOS from total aorta lysates from female mice (10A+/+ n=5, 10A-/- n=4, *P=0.0290). Mean measurements of 3-6 independent experiments are shown. (B-D) *p≤0.05; **p≤0.005; ***p≤0.0005 between cells transfected with non-silencing or ATP10A siRNA by 2-way ANOVA with Sidak's multiple comparison test, (F) P value by unpaired t-test.

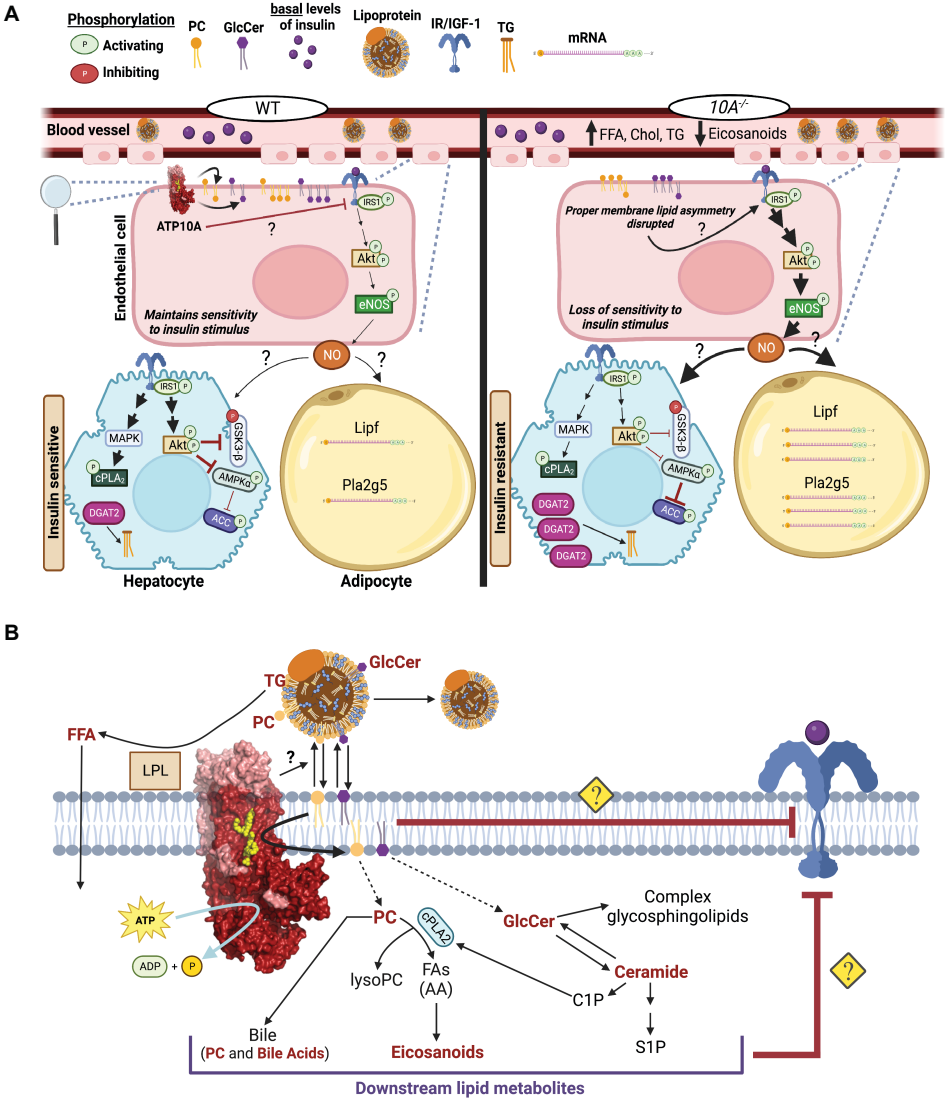


Figure 7. Model of ATP10A's role in metabolism. (A) Schematic illustrating ATP10A maintaining insulin sensitivity in ECs. Left panel: WT ATP10A in ECs blocks IR/IGF1R signaling, via an unknown mechanism, during basal levels of insulin and downstream of this; the tissues associated with the ECs (hepatocytes and adipocytes) also maintain their sensitivity to insulin. Right panel: When ATP10A is knocked out/down; ECs lose their sensitivity to insulin stimulus due to IR/IGF1R inappropriately responding to basal levels of insulin, downstream of this the tissues associated with the ECs could also lose their sensitivity to insulin stimulus (become insulin resistant). (B) Schematic illustrating ATP10A's proposed function specifically at the plasma membrane (what is being magnified by magnifying glass in (A)). ATP10A translocates PC and GlcCer from the outer leaflet to the inner leaflet, this could potentially affect how lipoproteins interact with the plasma membrane, the lipid platforms where proteins reside (insulin receptor), and the abundance of bioactive lipid species in the cytosolic space (that could also potentially affect IR/IGFR1 signaling). Schematics created using Biorender.com. LPL=lipoprotein lipase, NO=nitric oxide.

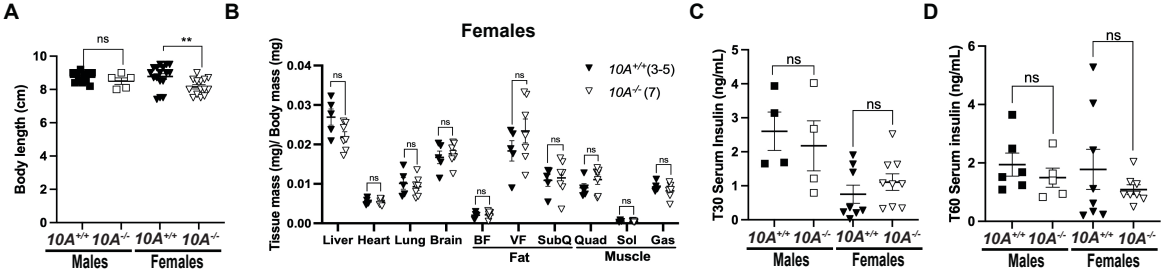


Supplemental Figure 1. Atp10A KO female mice have smaller bodies on the 12th week of the HFD. (A) Body length of mice was measured after CO2 sacrifice. P value by unpaired t-test, **P=0.0094. (Male: 10A+/+ n=11, 10A-/- n=5; Female: 10A+/+ n=17, 10A-/- n=14). (B)The wet mass of tissue was measured after removal from female mice on the 12th week on the HFD. Tissue mass is normalized to body mass. P value by unpaired t-tests. (10A+/+ n=3-5,10A-/- n=7). Insulin was measured from serum collected during the OGTT shown in Figure 1G,H at the (C) 30 minute time point (T30) and the (D) 60 minute time point (T60), P value by unpaired t-test. (Male: C: 10A+/+ n=4, 10A-/- n=4, D: 10A+/+ n=6, 10A-/- n=5; Female: 10A+/+ n=8, 10A-/- n=6).

| Females | 10A+/+ (WT) Average (n=7) | | | 10A-/- (KO) Average (n=13) | | | P-value (t-test, WT vs KO) | | |
|---|---|---|---|---|---|---|---|---|---|
| | Light | Dark | Full day | Light | Dark | Full day | Light | Dark | Full day |
| Avg. Daily Food intake (kcal/period) | 6.5 | 9.5 | 14.4 | 5.4 | 9.5 | 13.5 | ***0.0353 (*)*** | *0.9515 (ns)* | *0.4425 (ns)* |
| Avg. Daily Energy Expenditure (kcal/period) | 17.3 | 28.9 | 46.1 | 17.4 | 28.4 | 45.7 | *0.9596 (ns)* | *0.5622 (ns)* | *0.7033 (ns)* |
| Total Food (kcal) | 47.3 | 57.5 | 57.5 | 43.7 | 54.1 | 54.1 | *0.2807 (ns)* | *0.4428 (ns)* | *0.4428 (ns)* |
| O2 Consumption (ml/hr) | 102.9 | 125 | 115.5 | 103.3 | 123.1 | 114.6 | *0.8895 (ns)* | *0.5891 (ns)* | *0.7477 (ns)* |
| CO2 Production (ml/hr) | 81 | 98.1 | 90.8 | 80.3 | 95.9 | 89.2 | *0.7319 (ns)* | *0.4586 (ns)* | *0.5217 (ns)* |
| Energy balance (kcal) | 2.1 | 9.3 | 11.5 | -1.2 | 9.6 | 8.5 | ***0.0345 (*)*** | *0.9394 (ns)* | *0.4886 (ns)* |
| Resipiratory Exchange Ratio | 0.8 | 0.8 | 0.8 | 0.8 | 0.8 | 0.8 | *0.0839 (ns)* | *0.3642 (ns)* | *0.1761 (ns)* |
| Locomotor Activity (beam breaks/hr) | 121.5 | 269.9 | 206.3 | 100.9 | 266.1 | 195.3 | *0.2581 (ns)* | *0.8697 (ns)* | *0.5679 (ns)* |
| Pedestrian Locomotion (m) | 146.9 | 880.8 | 1027.7 | 141.1 | 843 | 984 | *0.8056 (ns)* | *0.7245 (ns)* | *0.7222 (ns)* |
| Distances in cage Locomotion (m) | 199.6 | 1017.4 | 1217 | 185.5 | 980.6 | 1166 | *0.5972 (ns)* | *0.7443 (ns* | *0.6956 (ns)* |

Supplemental Figure 2. Atp10A deletion causes alterations to average daily food intake and energy balance during the light hours in female mice fed a HFD for 13 weeks. The table indicates the parameters measured in the Sable System's Promethion Indirect Calorimetry System where the mice were single-housed. The values are an average measurement from 5 days in the system with ad libitum feeding. P value by unpaired t-test (10A+/+ n=7, 10A-/- n=13).

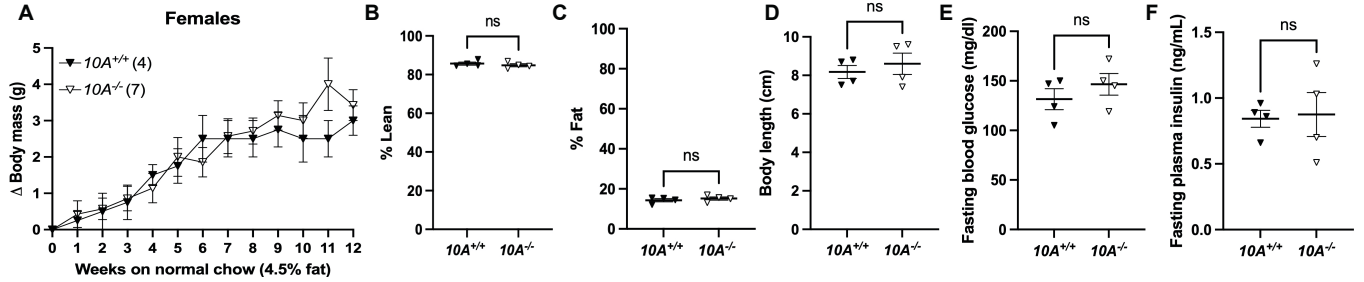


Supplemental Figure 3. Atp10A deletion does not affect weight gain, body composition, or glucose homeostasis in female mice after 12 weeks on normal chow. (A) Weight gain of 10A+/+ and 10A-/- female mice over the course of 12 weeks on normal chow (4.5 kcal% fat, Ad lib feeding), P value by 2-way ANOVA with Sidak's multiple comparison. (10A+/+ n=4,10A-/- n=7). (B) Lean and (C) fat body mass was normalized to the combined sum of lean and fat mass to calculate % Lean and % Fat mass. P value by unpaired t-test (10A+/+ n=4, 10A-/- n=4). (D) Body length of mice was measured after CO2 sacrifice. P value by unpaired t-test (10A+/+ n=4,10A-/- n=4). (E) Fasting blood glucose was measured a 5 hour fast, via a glucometer. P value by unpaired t-test (10A+/+ n=4,10A-/- n=4). (F) Fasting plasma insulin was measured after a 5 hour fast. P-value by unpaired t test (10A+/+ n=4,10A-/- n=4).

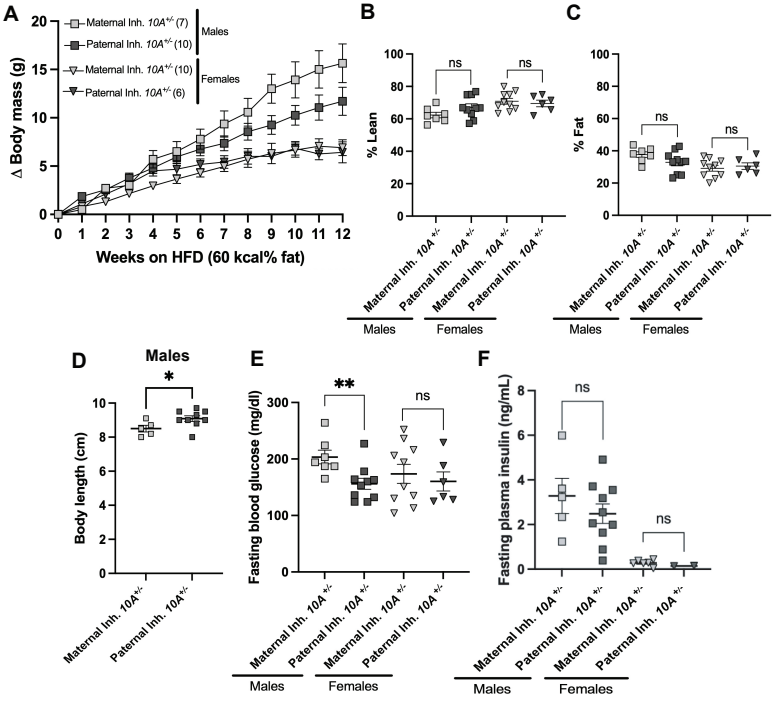


Supplemental Figure 4. Maternally inherited Atp10A deletion leads to smaller bodies and elevated fasting blood glucose in male mice on the 12th week on the HFD. (A) Weight gain of heterozygous males and females inheriting the KO allele maternally (Maternal Inheritance (Inh.), 10A+/- dam X 10A+/+ sire) or paternally (Paternal Inh, 10A+/+ dam x 10A+/- sire) over the course of 12 weeks on a HFD (60 kcal% fat, Ad lib feeding). P value by 2-way ANOVA with Sidak's multiple comparison. (Males: Maternal Inh.10A+/- n=7, Paternal Inh.10A+/- n=10; Females: Maternal Inh.10A+/- n=10, Paternal Inh.10A+/- n=6). (B) Lean and (C) fat body mass were normalized to the combined sum of lean and fat mass to calculate % Lean and % Fat mass. P value by unpaired t-test (Male: Maternal Inh.10A+/- n=7, Paternal Inh.10A+/- n=10; Female: Maternal Inh.10A+/- n=10, Paternal Inh.10A+/- n=6). (D) Body length of male mice was measured after CO2 sacrifice. P value by unpaired t-test, *P=0.0490. (Maternal Inh.10A+/- n=4, Paternal Inh.10A+/- n=9). (E) Fasting blood glucose was measured after a 5 hour fast, via a glucometer. P value by unpaired t-test, **P=0.0081. (Male: Maternal Inh.10A+/- n=7, Paternal Inh.10A+/- n=10; Female: Maternal Inh.10A+/- n=10, Paternal Inh.10A+/- n=6). (F) Fasting plasma insulin was measured after a 5 hour fast, P value by unpaired t-test. (Male: Maternal Inh.10A+/- n=6, Paternal Inh.10A+/- n=10; Female: Maternal Inh.10A+/- n=5, Paternal Inh.10A+/- n=2).

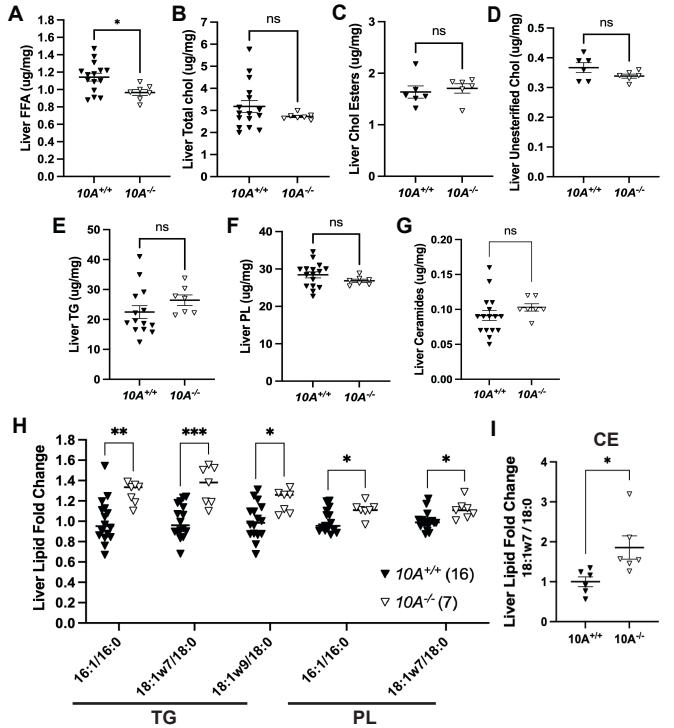


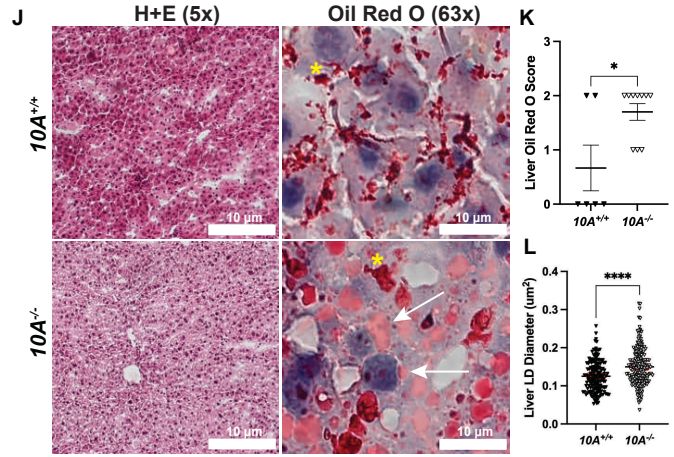


Supplemental Figure 5. Atp10A deletion causes changes to liver lipid metabolism in female mice after 12 weeks on a HFD. (A-G) FFAs, Total cholesterol, cholesterol esters, unesterifed cholesterol, TGs, PLs, and ceramides were measured from flash frozen livers via gas chromatography. Livers were collected after a 5 hour fast or after a 5 hour fast followed by an OGTT. P value by unpaired t-test (FFA: 10A+/+ n=15,10A-/- n=7, *P=0.0201; Total cholesterol: 10A+/+ n=16, 10A-/- n=7; Cholesterol esters: 10A+/+ n=6,10A-/- n=6; Unesterified cholesterol: 10A+/+ n=6,10A-/- n=6; TG: 10A+/+ n=14, 10A-/- n=7; PLs: 10A+/+ n=16, 10A-/- n=7; Ceramides: 10A+/+ n=16, 10A-/- n=7). The saturation of liver (H) TG, PL, and (I) CE species was determined by gas chromatography. The fold change of unsaturated vs saturated TG, PL, CE is shown. P value by 2-way ANOVA with Sidak's multiple comparison, TG: **P=0.0025, ***P=0.0001, *P=0.0443, PL: *P=0.0297, *P=0.0281 (10A+/+ n=16, 10A-/- n=7). CE: P value by unpaired t-test, *P=0.0223 (10A+/+ n=6, 10A-/- n=6). (J) Representative images of livers stained with H+E (5x) or Oil Red O (63x). The coalescence of the Oil Red O stain is indicated by yellow asterisks (artifact) and the arrows point to neutral lipids stained by Oil Red O. Scale bars = 10 µM. (K) Liver sections were scored using the Oil Red O Score described in the Materials and Methods. P value by nonparametric t-test (Mann-Whitney U), *P=0.0327 (10A+/+ n=6, 10A-/- n=10). (L) The diameters of Oil Red O positive lipid droplets (LD) in the liver sections with a score of 2 were measured using ImageJ. The red line in the graph represents the SEM. P value by unpaired t-test, ****P=<0.0001 (10A+/+,120 LDs measured, n=2, 10A-/-, 203 LDs measured, n=3).

A

| Peptides | 1A, 1B | 3A,3B | 5A,5B |
|---|---|---|---|
| Amino acid number | 27-38 | 41-53 | 498-509 |
| Amino acid sequence | RTRTVRSNLLPP | TEDSTIGAPKGER | HKTQSIKSHRRT |

B

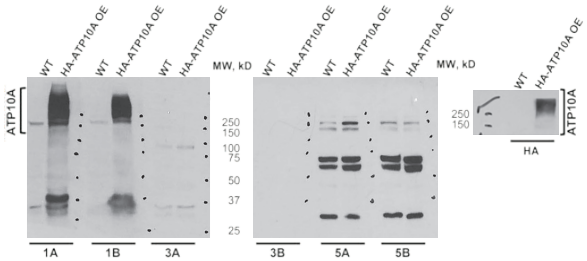


C

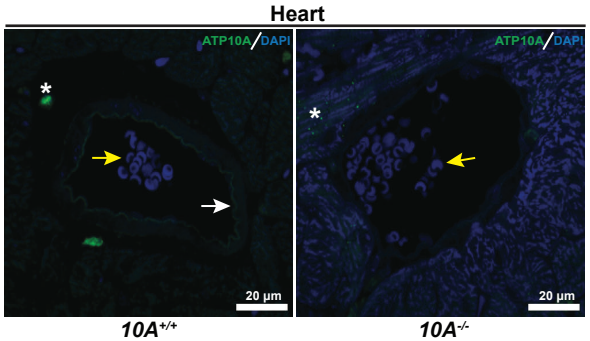


Supplemental Figure 6. Validation of anti-ATP10A antibody: expression of ATP10A in HeLa cells with over-expressed HA-ATP10A and in mouse heart. (A) Table indicating the sequences of the ATP10A peptides that were injected into rabbits to produce antibodies. (B) Representative images of total cell lysates from HeLa cells with over-expressed HA-ATP10A (40 µg total protein) that were subjected to Western immunoblot analyses for expression of ATP10A using antibody produced against ATP10A peptides (left and central panels) and HA (right panel). (C) Representative immunofluorescent images of hearts from female mice showing expression of ATP10A (green) and DAPI (blue). Scale bar = 20 µm. The white asterisk indicates background staining, the white arrow indicates ATP10A positive staining, the yellow arrow indicates auto fluorescent red blood cells (10A+/+ n=1, 10A-/- n=1).

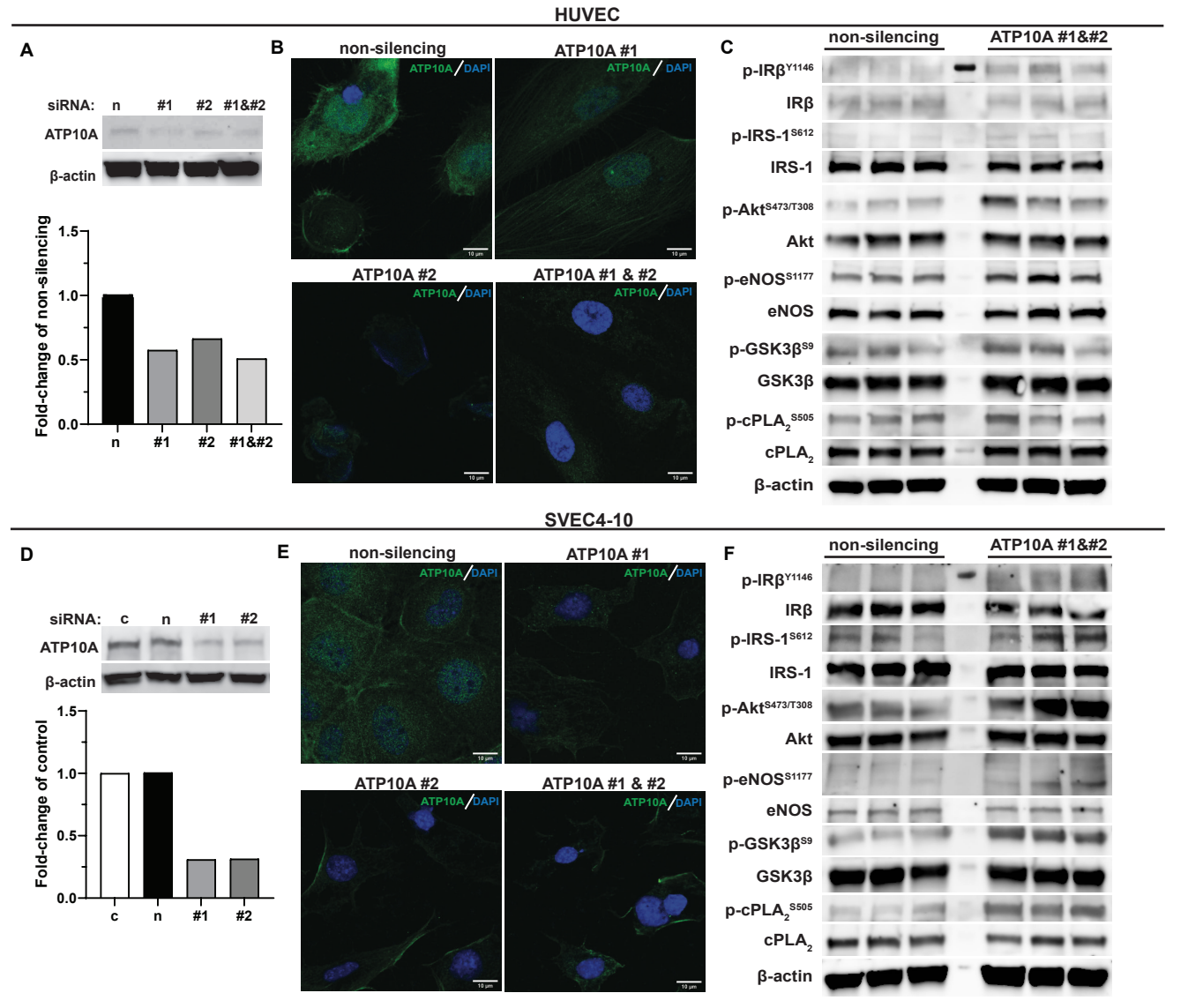


Supplemental Figure 7. ATP10A expression level regulates basal activity of insulin signaling pathways in endothelial cells. (A,D) Representative images and quantitative analysis of ATP10A from immunoblots of HUVEC (A) and SVEC4-10 (D) untreated (c), transfected with non-silencing siRNA or ATP10A siRNA constructs (#1, #2, #1&#2). (B, E) Representative immunofluorescent images showing expression of ATP10A and DAPI in HUVEC (B) and SVEC4-10 (E) transfected with non-silencing siRNA (n) or ATP10A siRNA constructs (ATP10A#1, ATP10A#2, ATP10A#1&#2). Scale bar=10 μm. (C, F) Representative images of basal phosphorylated and total IRβ, IRS-1, Akt, eNOS, GSK-3β, and cPLA2 from immunoblots of HUVEC (C) and SVEC4-10 (F) transfected with non-silencing siRNA or ATP10A#1&#2 siRNA constructs. Note that the lane between the non-silencing and ATP10A#1&#2 treated lanes contains the molecular weight marker.

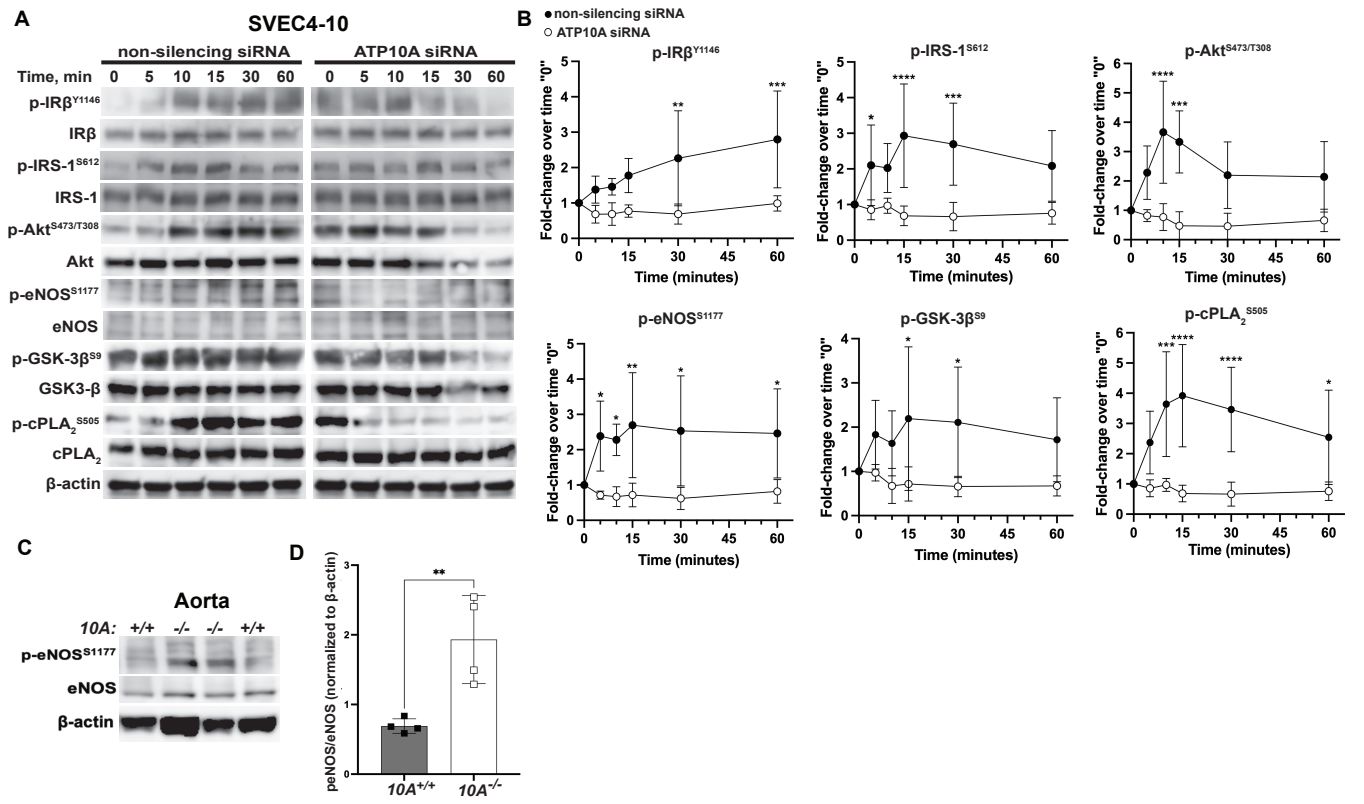


Supplemental Figure 8. ATP10A expression regulates insulin signaling pathway in SVEC4-10 cells and mouse aorta. (A) Representative images and (B) quantitative analysis from immunoblots of phosphorylated and total IRβ, IRS-1, Akt, eNOS, GSK-3β, and cPLA2 from SVEC4-10 cells transfected with non-silencing siRNA or ATP10A siRNA constructs and then treated with insulin for 0-60 mins. Mean measurements of 3-6 independent experiments are shown. *p≤0.05; **p≤0.005; ***p≤0.0005; ***p≤0.0001 between cells transfected with non-silencing or ATP10A siRNA by 2-way ANOVA with Sidak's multiple comparison test. (C) Representative blots and (D) quantitative analysis from immunoblots of phosphorylated and total eNOS from total aorta lysates from male mice (10A+/+ n=2, 10A-/- n=4, statistics were not done due to low n). Mean measurements of 3-6 independent experiments are shown.

Supplemental Table 2

# Gene Enrichment Report

## **Table 1:** pathway KEGG

| geneSet | description | link | size | overlap | expect | enrichmentRatio | pValue | FDR |
|---|---|---|---|---|---|---|---|---|
| mmu04972 (http://www.kegg.jp/kegg-bin/show_pathway?mmu04972+13487+18784+232680+27222+432530) | Pancreatic secretion | Table 2 | 103 | 5 | 0.8090634 | 6.179985 | 0.0012387 | 0.3938938 |
| mmu00730 (http://www.kegg.jp/kegg-bin/show_pathway?mmu00730+11636+11647) | Thiamine metabolism | Table 3 | 15 | 2 | 0.1178248 | 16.974359 | 0.0059725 | 0.5667857 |
| mmu04080 (http://www.kegg.jp/kegg-bin/show_pathway?mmu04080+110902+11555+12672+13488+14765+19222+23796) | Neuroactive ligand-receptor interaction | Table 4 | 289 | 7 | 2.2700906 | 3.083577 | 0.0072516 | 0.5667857 |
| mmu05150 (http://www.kegg.jp/kegg-bin/show_pathway?mmu05150+13510+20344+225256) | Staphylococcus aureus infection | Table 5 | 56 | 3 | 0.4398792 | 6.820055 | 0.0095348 | 0.5667857 |
| mmu00561 (http://www.kegg.jp/kegg-bin/show_pathway?mmu00561+235582+67717+68393) | Glycerolipid metabolism | Table 6 | 61 | 3 | 0.4791541 | 6.261034 | 0.0120409 | 0.5667857 |
| mmu04964 (http://www.kegg.jp/kegg-bin/show_pathway?mmu04964+27222+76257) | Proximal tubule bicarbonate reclamation | Table 7 | 22 | 2 | 0.1728097 | 11.573427 | 0.0126837 | 0.5667857 |
| mmu04145 (http://www.kegg.jp/kegg-bin/show_pathway?mmu04145+12845+14997+17167+17534+242341) | Phagosome | Table 8 | 181 | 5 | 1.4217523 | 3.516787 | 0.0135801 | 0.5667857 |
| mmu00790 (http://www.kegg.jp/kegg-bin/show_pathway?mmu00790+11647+216343) | Folate biosynthesis | Table 9 | 26 | 2 | 0.2042296 | 9.792899 | 0.0174897 | 0.5667857 |
| mmu04976 (http://www.kegg.jp/kegg-bin/show_pathway?mmu04976+13849+27222+432530) | Bile secretion | Table 10 | 71 | 3 | 0.5577039 | 5.379198 | 0.0180930 | 0.5667857 |
| mmu00650 (http://www.kegg.jp/kegg-bin/show_pathway?mmu00650+268860+272428) | Butanoate metabolism | Table 11 | 27 | 2 | 0.2120846 | 9.430199 | 0.0187942 | 0.5667857 |

## **Table 2:** Significantly differential expressed genes in Pancreatic secretion

| | Feature_gene_name | baseMean | pvalue | padj | FoldChange |
|---|---|---|---|---|---|
| ENSMUSG00000041193.15 | Pla2g5 | 327.69290 | 0.0000000 | 0.0000000 | 21.6047666 |
| ENSMUSG00000007107.6 | Atp1a4 | 258.59064 | 0.0000000 | 0.0000010 | 4.8748642 |
| ENSMUSG00000071553.10 | Cpa2 | 196.02196 | 0.0000000 | 0.0000012 | 3.7086972 |
| ENSMUSG00000020431.5 | Adcy1 | 104.91067 | 0.0002204 | 0.0205006 | 0.3598145 |
| ENSMUSG00000001225.12 | Slc26a3 | 29.11604 | 0.0002398 | 0.0212087 | 3.9715976 |

## **Table 3:** Significantly differential expressed genes in Thiamine metabolism

| | Feature_gene_name | baseMean | pvalue | padj | FoldChange |
|---|---|---|---|---|---|
| ENSMUSG00000026817.14 | Ak1 | 1358.0322 | 0.0002921 | 0.0231430 | 2.018769 |
| ENSMUSG00000028766.10 | Alpl | 237.0382 | 0.0005178 | 0.0342469 | 2.843773 |

## **Table 4:** Significantly differential expressed genes in Neuroactive ligand-receptor interaction

| | Feature_gene_name | baseMean | pvalue | padj | FoldChange |
|---|---|---|---|---|---|
| ENSMUSG00000056380.13 | Gpr50 | 56.43242 | 0.0000147 | 0.0038591 | 571.2601672 |
| ENSMUSG00000040495.4 | Chrm4 | 14.01271 | 0.0000269 | 0.0056257 | 25.0694979 |
| ENSMUSG00000043017.9 | Ptgir | 400.58672 | 0.0000513 | 0.0081485 | 2.3456060 |
| ENSMUSG00000044338.9 | Aplnr | 803.32162 | 0.0007599 | 0.0429697 | 2.7616563 |
| ENSMUSG00000021478.6 | Drd1 | 52.58807 | 0.0008995 | 0.0482169 | 0.2768258 |
| ENSMUSG00000022041.10 | Chrna2 | 169.09289 | 0.0009182 | 0.0488542 | 2.1544465 |
| ENSMUSG00000045730.4 | Adrb2 | 637.53597 | 0.0009437 | 0.0496613 | 0.4256661 |

## **Table 5:** Significantly differential expressed genes in Staphylococcus aureus infection

| | Feature_gene_name | baseMean | pvalue | padj | FoldChange |
|---|---|---|---|---|---|
| ENSMUSG00000069441.3 | Dsg1a | 61.66929 | 0.0000004 | 0.0002329 | 5.596025 |
| ENSMUSG00000061928.6 | Dsg1b | 20.82076 | 0.0000261 | 0.0056199 | 19.302742 |
| ENSMUSG00000026580.16 | Selp | 210.55678 | 0.0007295 | 0.0421402 | 2.465355 |

## **Table 6:** Significantly differential expressed genes in Glycerolipid metabolism

| | Feature_gene_name | baseMean | pvalue | padj | FoldChange |
|---|---|---|---|---|---|
| ENSMUSG00000024768.5 | Lipf | 231.5996 | 0.0000000 | 0.0000000 | 16.1785033 |
| ENSMUSG00000012187.13 | Mogat1 | 674.7383 | 0.0002415 | 0.0212126 | 0.4207309 |
| ENSMUSG00000020258.16 | Glyctk | 130.4926 | 0.0002809 | 0.0226372 | 2.2850670 |

## **Table 7:** Significantly differential expressed genes in Proximal tubule bicarbonate reclamation

| | Feature_gene_name | baseMean | pvalue | padj | FoldChange |
|---|---|---|---|---|---|
| ENSMUSG00000007107.6 | Atp1a4 | 258.5906 | 0.0000000 | 0.0000010 | 4.874864 |
| ENSMUSG00000010064.15 | Slc38a3 | 708.3462 | 0.0008828 | 0.0480317 | 2.559326 |

## **Table 8:** Significantly differential expressed genes in Phagosome

| | Feature_gene_name | baseMean | pvalue | padj | FoldChange |
|---|---|---|---|---|---|
| ENSMUSG00000031849.9 | Comp | 138.8050 | 0.0000680 | 0.0096990 | 2.5941413 |
| ENSMUSG00000020695.14 | Mrc2 | 2506.8921 | 0.0001199 | 0.0138293 | 2.7056454 |
| ENSMUSG00000067201.11 | H2-M9 | 240.8505 | 0.0001812 | 0.0177730 | 0.4219105 |
| ENSMUSG00000028238.6 | Atp6v0d2 | 208.2672 | 0.0001948 | 0.0184835 | 4.0684324 |
| ENSMUSG00000026390.7 | Marco | 155.7569 | 0.0006129 | 0.0371291 | 2.3528541 |

## **Table 9:** Significantly differential expressed genes in Folate biosynthesis

| | Feature_gene_name | baseMean | pvalue | padj | FoldChange |
|---|---|---|---|---|---|

| | | | | | |
|---|---|---|---|---|---|
| ENSMUSG00000006764.8 | Tph2 | 959.1933 | 0.0000001 | 0.0000516 | 22.049261 |
| ENSMUSG00000028766.10 | Alpl | 237.0382 | 0.0005178 | 0.0342469 | 2.843773 |

## **Table 10:** Significantly differential expressed genes in Bile secretion

| | Feature_gene_name | baseMean | pvalue | padj | FoldChange |
|---|---|---|---|---|---|
| ENSMUSG00000007107.6 | Atp1a4 | 258.5906 | 0.0000000 | 0.0000010 | 4.8748642 |
| ENSMUSG00000038776.13 | Ephx1 | 4746.0156 | 0.0000094 | 0.0027610 | 2.0548225 |
| ENSMUSG00000020431.5 | Adcy1 | 104.9107 | 0.0002204 | 0.0205006 | 0.3598145 |

## **Table 11:** Significantly differential expressed genes in Butanoate metabolism

| | Feature_gene_name | baseMean | pvalue | padj | FoldChange |
|---|---|---|---|---|---|
| ENSMUSG00000057880.12 | Abat | 3895.093 | 0.0000001 | 0.0000484 | 2.4992921 |
| ENSMUSG00000030972.6 | Acsm5 | 1971.103 | 0.0004816 | 0.0326044 | 0.4485598 |